Multi-hazard risk assessment in Adana, Turkey

A GIS analysis of earthquake, flood and landslide risk on the Southern Mediterranean coast of Turkey

Master Thesis

Deniz Gijsel – student number: 6954537

Utrecht University

First supervisor: Prof. Dr. Steven de Jong

Second supervisor: Dr. Tjalling de Haas

Universiteit Utrecht

Utrecht University

Master's Degree Thesis

Multi-hazard risk assessment in Adana, Turkey

Author:

Deniz Gijsel

Supervisors:

Prof. Dr. Steven de Jong (first supervisor)

Dr. Tjalling de Haas (second supervisor)

Thesis submitted in partial fulfilment of the requirements for the degree of

Master of Science in Earth Surface and Water, Geohazards and Earth Observation

30 European Credits (EC)

January 22, 2021

Abstract

The province of Adana, located in southern Mediterranean Turkey, has been exposed to multiple types of natural hazards in the past. The most prominent hazards present in this area are earthquakes, floods and landslides. In this area, studies have mainly focused on individual events or on specific locations. An overarching framework of the multi hazards and their feedbacks, which is crucial in minimalizing losses and city planning, is missing. This research is aimed to estimate earthquake, flood and landslide hazard and risk. The estimation is done by calculating hazard separately for the three hazard types, including their feedbacks and interaction with other hazards. After these calculations, risk was estimated by applying the calculated hazard to a damage equation, resulting in three maps representing monetary values of loss.

The results for earthquake hazard show that the southern part of the study area is dominated by high peak ground acceleration (PGA) values, while a decrease in value occurs when going northwards. Increasing the magnitude fades the circular buffer zones around historical hypocentra with high PGA values in the south. The flood hazard map indicates that the steep and elevated north and south east contain little to no hazard, while the flat and fertile south contains most hazard. The same steep slopes, which were also noticeable in the flood hazard map, can be seen in the north and eastern part in the landslide hazard map, since these account for most of the unstable pixels. All risk maps have a very similar pattern based on the land use distribution of the study area. Differences between the hazards are the spatial distribution of high value pixels within the urban environments and the fact that landslides are less dependent on land use distribution patterns.

The methodology and data used for this research is excellent for assessing risk on a relatively large scale. Land use can be obtained globally on a high resolution. Combining the calculated hazard with the widely available and accessible land cover data is a great alternative for when the study area is large or when data is scarce. However, availability and accessibility have a negative relationship with accuracy, especially with landslide risk assessment. Studies making use of building inventories or other intensive data to estimate risk show more accurate results on a higher resolution. Many risk assessments are conducted making use of this methodology, but few use a multi-hazard approach or are executed on a large scale. Using a multi-hazard approach on this scale will provide new insights in land use planning, hazard adaptation, hazard prevention and hazard mitigation.

Table of Contents

1. Introduction

Although the number of fatalities resulting from natural hazard varies strongly from year to year, the extent of the impact of natural hazards on earth is undeniable. In the past decade, an average of 60.000 people die yearly from natural disasters, which accounts for 0.1 percent of global deaths. While the absolute costs caused by natural hazards seems to increase with the years (figure 1), the losses as a share of GDP seem to vary yearly between 0.15 and 0.5 percent of global GDP (Ritchie & Roser, 2019). On top of these fatalistic statistics, the world must deal with the possibility that the frequency and magnitude of natural hazards will increase in the future, according to the most recent IPCC reports. These consequences of climate changes will however not be felt evenly across the globe. There will be a clear distinction between winners and losers concerning the changes in severity of natural hazards (O'Brien & Leichenko, 2003). Even though evidence for human induced climate change is there, it is however hard to measure how much this is influencing extreme events. Still, a warming climate results in more energy and therefore more weather-related activity on earth, and the consensus is that this will change the shape of probability distributions of several natural hazards in the future (McBean, 2004) (IPCC, 2012). An easier way of seeing what effect time has on the influence of natural hazards is by comparing insured losses over time. A normal ratio of global insured to uninsured losses is forty percent and since the beginning of the nineties this ratio has almost always been well over forty percent (Munich Re, 2019). With the increase in insured losses in combination with exponential increase of population size and damageable goods, the impact of natural disasters on earth will only grow in the future (figure 1) (Keller & DeVecchio, 2015).

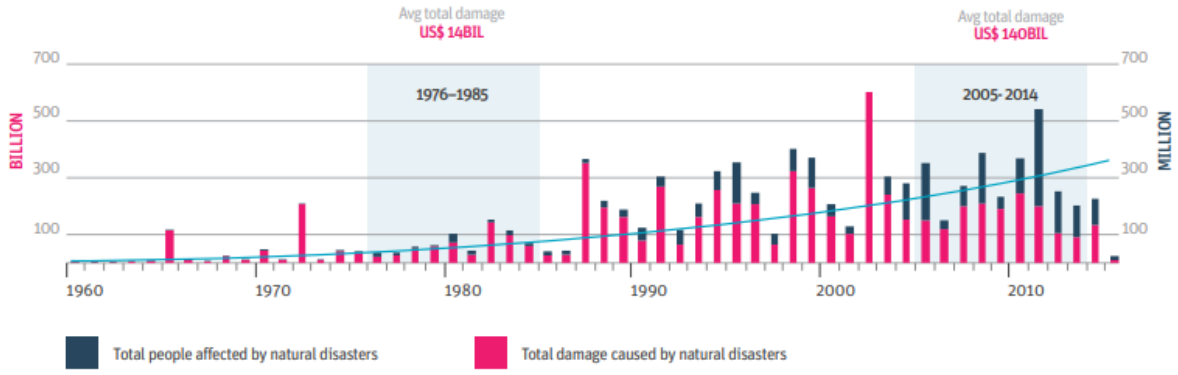

Figure 1. Due to urbanization, increase of population size, damageable goods and climate change, the impact of natural hazards will only grow in the future (Global Facility for Disaster Reduction and Recovery, 2016).

The province of Adana, located in southern Mediterranean Turkey (figure 2), has been exposed to multiple types of natural hazards in the past. Being located directly above the Eastern Anatolian Fault Zone (EAFZ), the city of Adana is extremely prone to earthquakes. A well-known example is the earthquake of 1998, when 145 people lost their lives and total damages were estimated to be 1.3

billion USD. Widespread liquefaction, sand boils, ground fissures and ground deformation occurred during this earthquake, causing these severe damages and losses of life (Kuru & Ulusay, 2004). Not only earthquakes are terrorizing the area. Both flash floods and river floods caused serious losses. The very recent flash flood in December 2019, caused by 250 mm of rain in less than three days, resulted in severe damages in several districts of the city (Demirören News Agency, 2019). Also landslides have struck the area in the past, of which the most extreme event taking place in 2001 (Sivrikaya, et al., 2008), and droughts, which are less event-defined but still causing insidious natural hazard and serious harm in the area (Cetin, et al., 2018).

1.1 Research objective

In this area, studies have mainly focused on the individual events or on specific locations (Sivrikaya, et al., 2008) (Kuru & Ulusay, 2004) (Aktar, et al., 2000) (Leventeli, 2016). An overarching framework of the multi-hazards and their feedbacks, which is crucial in minimalizing losses and city planning (Kappes, et al., 2012), is missing. An example of one of these feedbacks is that earthquakes may trigger landslides, which may block rivers with natural dams, increasing the chance of flooding and the risk of levee breaches. These type of chain reactions are crucial in defining natural hazard risk (Fan, et al., 2019). Separate studies of single hazard processes might give an incomplete overview of the actual situation and may not yield the right land management information. Risk reduction from one hazard may cause an increase in risk from another hazard. A multi-hazards approach and survey may avoid such risk (Finlay & Fell, 1997). In the past decades, the limitation of single hazard studies has been highlighted in several studies (Gill & Malamud, 2014) (Terzi, et al., 2019). Assessing single-hazard risk is very data demanding and time consuming. Also, it is hard to compare results of single-hazard studies since these are conducted by making use of different methodologies (Kappes, et al., 2012). The relatively large scale of hazard and risk assessment is beneficial for city planners and mitigation measurements. However, this also influences data demand and accuracy of the assessment (Delmonaco, et al., 2003).

A multi-hazard risk assessment is different from a normal risk assessment in several ways, of which the most important difference is the already described cascade concept. A multi-hazard approach, integrating all present natural hazard types in one single methodology, saves time and requires less data. In this project, the multi-hazard risk situation in the province around the city of Adana is considered and multiple hazards are investigated for the Adana area. The goal of this study is to estimate earthquake, flood and landslide hazard and risk. To do so, hazard will be calculated separately for the three hazard types, with some hazards including feedbacks and interaction with other hazards. The output of hazards will be presented in three maps, one for each hazard respectively, which represent the spatial distribution of hazard. After these calculations, risk will be estimated by applying

hazard to a damage equation, resulting in three maps representing monetary values of loss. In the discussion, all six maps will be explained, interpreted, implicated and compared to existing literature.

2. Study Area

The Adana province is the sixth largest province in Turkey, containing an estimate of 2.2 million people in 2020 according to the Turkish Statistical Institute. The city of Adana bids home to 79 percent of all residents in the province and is centered in the Cilicia plain, a fertile and flat region located south of the Taurus mountains. The province consists of 15 districts of which four contain parts of the city. In descending order of population size these provinces are Seyhan, Yüreğir, Çukurova and Sarıçam (figure 2).

Figure 2. The Cilician plain, located south of the Taurus mountains. Outlined are the four districts that contain parts of the city of Adana.

2.1 Historic events

The people of Adana have experienced a substantial number of natural catastrophes. To get insight in why and how these catastrophes happened, an inventory of events is made. Since the region is located directly above the intersection between the Eastern Anatolian Fault Zone (EAFW) and the Dead Sea Transform, Adana is extremely prone to earthquakes with a medium to large magnitude. Since 1970, twelve earthquakes with a magnitude of 6.0 or higher occurred on the EAFW according to the USGS Comprehensive Catalog, of which the most severe took place in 1998. This earthquake (M_s of 6.2) resulted in a loss of 145 lives, 1500 injured and total damages were estimated to be 1.3 billion USD.

Due to the source depth and thickness of alluvial deposits, there was no observed surface rupture. The only visible geological markers left by this earthquake were sand boils due to liquefaction (Kuru & Ulusay, 2004).

Adana is situated in the Ceyhan and Seyhan river basin. North of the city, the Seyhan Dam's main goal used to be producing hydroelectric power, which made the city's economy grow in the 1950s (Tozoglu, 2020). However, flood control was a sub target, since the floods of 1947 and 1948 proved the then newly built flow regulator structure to be insufficient (Tanoğlu, 1943). After heavy rainfall in November 1947, the Seyhan river flooded and over 200 people drowned (The Courier-Mail, 1947). As of right now, the main purpose of the dam has shifted from power production to flood control and irrigation development. However, in recent years flooding has been a problem for the area as well. November and December have proven to be very wet months in the past years, causing severe flooding on Christmas 2019. The central districts of the city received around 249mm of rainfall in 48 hours. Eight people were injured and damages to both housing and agriculture are still being assessed (Hürriyet, 2019).

Landslides tend to occur as a result of heavy rainfall or earthquakes and cause 27% of total damages to buildings out of all natural hazards, which makes landslides the second most destructive hazard after earthquakes in Turkey. During December 2001, a total of 325mm of precipitation fell on the Adana city area. The soil became heavily saturated and lost its strength. Buildings located on the steep slope where the landslide occurred were destroyed and buildings on top of the slope were cracked heavily due to discontinuities and settlements. The landslide caused damage to around 250 buildings and affected 25,000 people (Sivrikaya, et al., 2008).

2.2 Climate

Adana is located on the Cilicia plain south of the Taurus Mountains. The climate is strongly influenced by topography. The northern part of the province is characterized by steep and harsh mountains, while the south can be distinguished by flat, arable lands. Therefore, the north tends to lean towards the Central Anatolian climate, which is generally colder and wetter than the Mediterranean climate observed in the south. The city of Adana deals with dry and hot summers and warm and wet winters (figure 3).

The mean observed precipitation in the city of Adana is 663mm per year. However, precipitation varies highly throughout the 4 districts. Precipitation tends to increase along with elevation. Therefore, the harsh mountainous north generally suffers from more rainfall than the southern planes.

The average temperature in the city of Adana is 19.3 °C. August is the warmest month averaging 28.6 °C, while January is the coldest month averaging 9.5 °C (Climate Data, 2020).

Rainfall is the single most important triggering factor concerning floods and landslides. Evaluating climate and climate variability helps assessing the cause, frequency and intensity of natural hazards (Polemio & Petrucci, 2000) (Hong, et al., 2007).

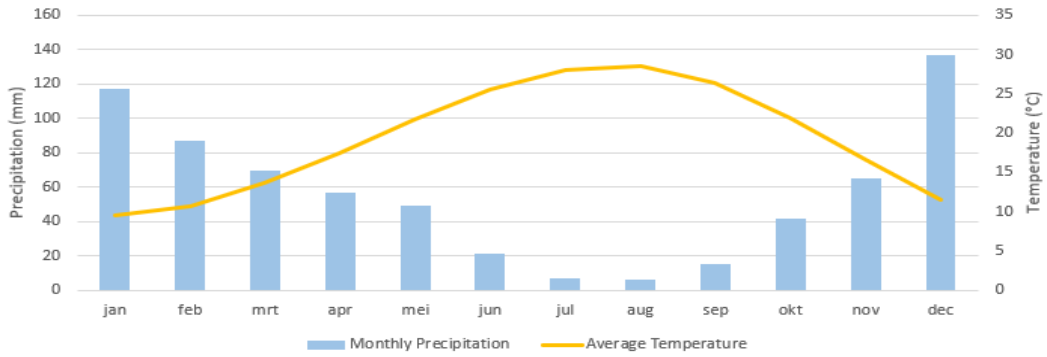

Figure 3. Monthly precipitation and average temperature (Climate Data, 2020).

Geology

Focusing on the four districts, the most recent geological unit can be found in the southern two districts: Yüreğir and Seyhan. Alluvium makes up most of the soil, which are Holocene depositions originating from the Seyhan river. Moving north towards the reservoir, harder materials can be found. Examples are hardened calcium carbonate binding gravel, sand and clay, of which the latter are deposited in river terraces in the upper Pleistocene (Cipollari, et al., 2013). North of this unit, the Handere Formation can be found (ca. 5.45 to 5.33 Ma). This formation consists of fluvial conglomerates and marls (Radeff, et al., 2017). North of the reservoir, the sandstones of the Kuzgun formation can be found (figure 4) (Cipollari, et al., 2013).

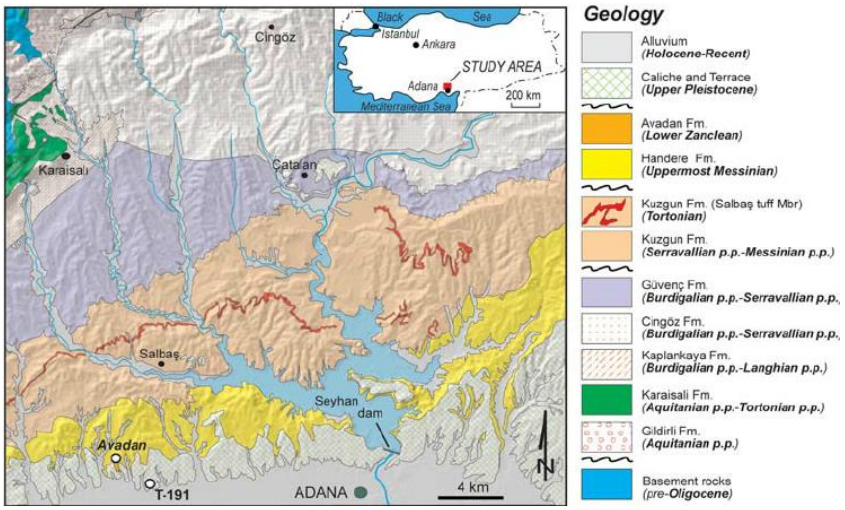

Figure 4. Geology map surrounding the Adana reservoir. The area out of the scope of this map is homogeneous with what is displayed here (Cipollari, Schildgen, & Cosentino, 2013).

Looking at soil, three different types can be distinguished in the Adana area (ISRIC, 2020). In the most northern part of the four provinces, leptosols can be found. Leptosols are soils with very shallow profile depth containing large amounts of gravel. Leptosols often indicate areas with very little soil-forming processes. Going further south, these soil-forming processes become more common. South of the leptosols, surrounding the reservoir and most of the city, are the luvisols. Luvisols are already far more suitable for agriculture because of their high nutrient content and good drainage. The most southern part of the area consists of vertisols (figure 5). These soils are soft and thick compared to luvisols and leptosols. The soft- and thickness of soils play important roles in both the calculation of landslide and flood hazard. Since geology and soil composition influence earthquake and landslide triggering (Pearce & O'Loughlin, 1985) and effects (Bauer, et al., 2001), the local geological and soil patterns should be assessed accordingly. Different geological and soil patterns can cause different peak ground accelerations and land slide safety factors, which would have different effects on the environment.

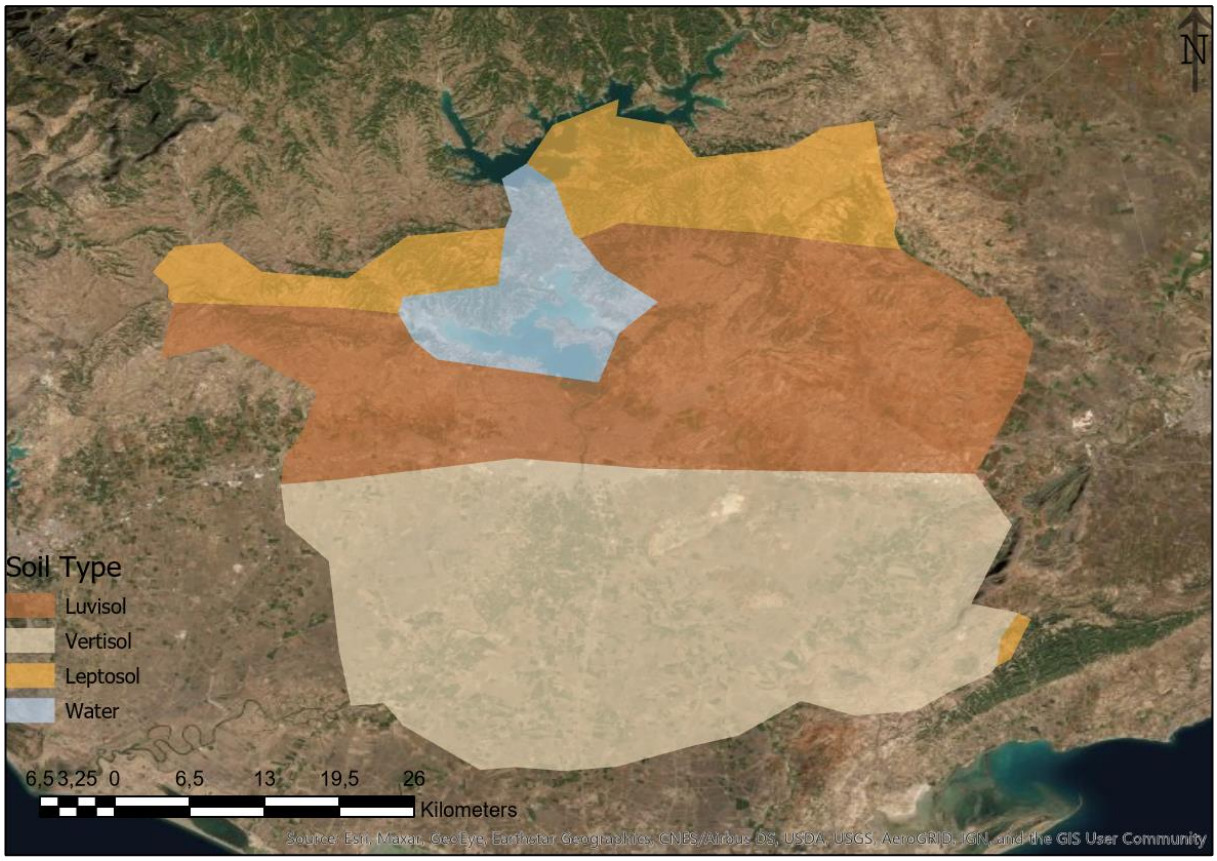

Figure 5. Soil type distribution over the study area (ISRIC, 2020).

2.4 Topography

The three-dimensional arrangement of Adana's physical attributes is shaped in a very recognizable pattern. From north to south, elevation decreases severely. The Taurus mountains, which form the coastline in the west, move northwards around the Adana area. This leaves a low lying plain south of the mountains. Topography, geology and land use influence and interact with each other. The low-

lying plains in the south leave room for thick soils which are very productive for agricultural purposes. Steep slopes can also be found in the south eastern part of the region, which increases the proneness for landslides in that part. A digital elevation model of the area is displayed in figure 6.

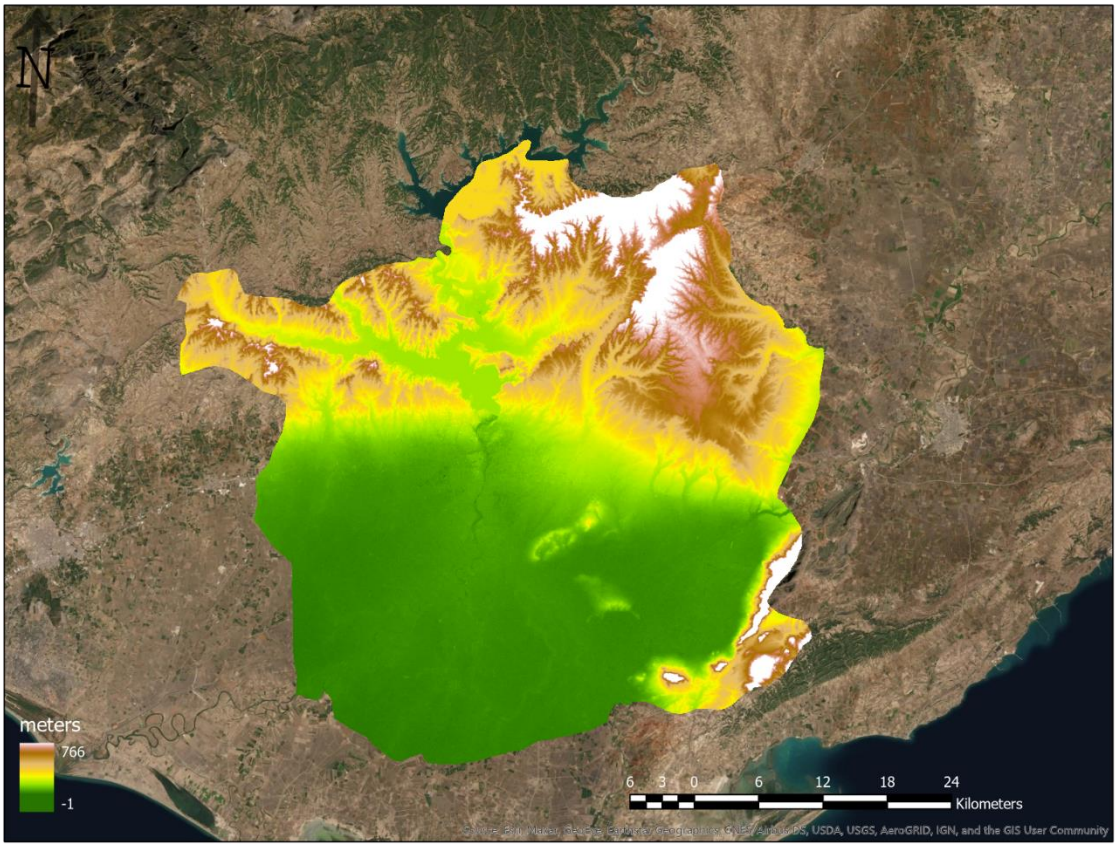

Figure 6. Digital elevation model of the study area obtained from the ASTER sensor.

2.5 Land use

Risk and hazard play a crucial but complex role in most developed countries when planning land use (Boholm, 2008). It is therefore important to thoroughly map land use when examining environmental risk. The four districts have a total surface of 2333 square kilometers. To distinct the different land use classes, the Corine Land Cover 2018 dataset was obtained from the Copernicus Land Monitoring Service. Since the Cilicia plain is extremely fertile, it is no surprise that over 75 percent of the area has an agricultural purpose, of which 40 percent is permanently irrigated. Only six percent is considered urban fabric, of which just over five square kilometers are distinguished as discontinuous urban fabric (table 1). Land use is crucial in defining the elements at risk and therefore the vulnerability of a specific study area. Land use relies heavily on soil composition. Most agriculture is conducted in the thick clayey soils in the south, while the norths' thin hard soils remain uninhabited (figure 7).

Table 1. Land use classes in 2018. Data obtained from Copernicus Land Monitoring Service.

LAND USE CLASS	2018 (KM^2)
URBAN	146
INDUSTRIAL	79
INFRASTRUCTURE	16
AGRICULTURE	1755
FOREST	180
SHRUBLANDS	56
WATER	102

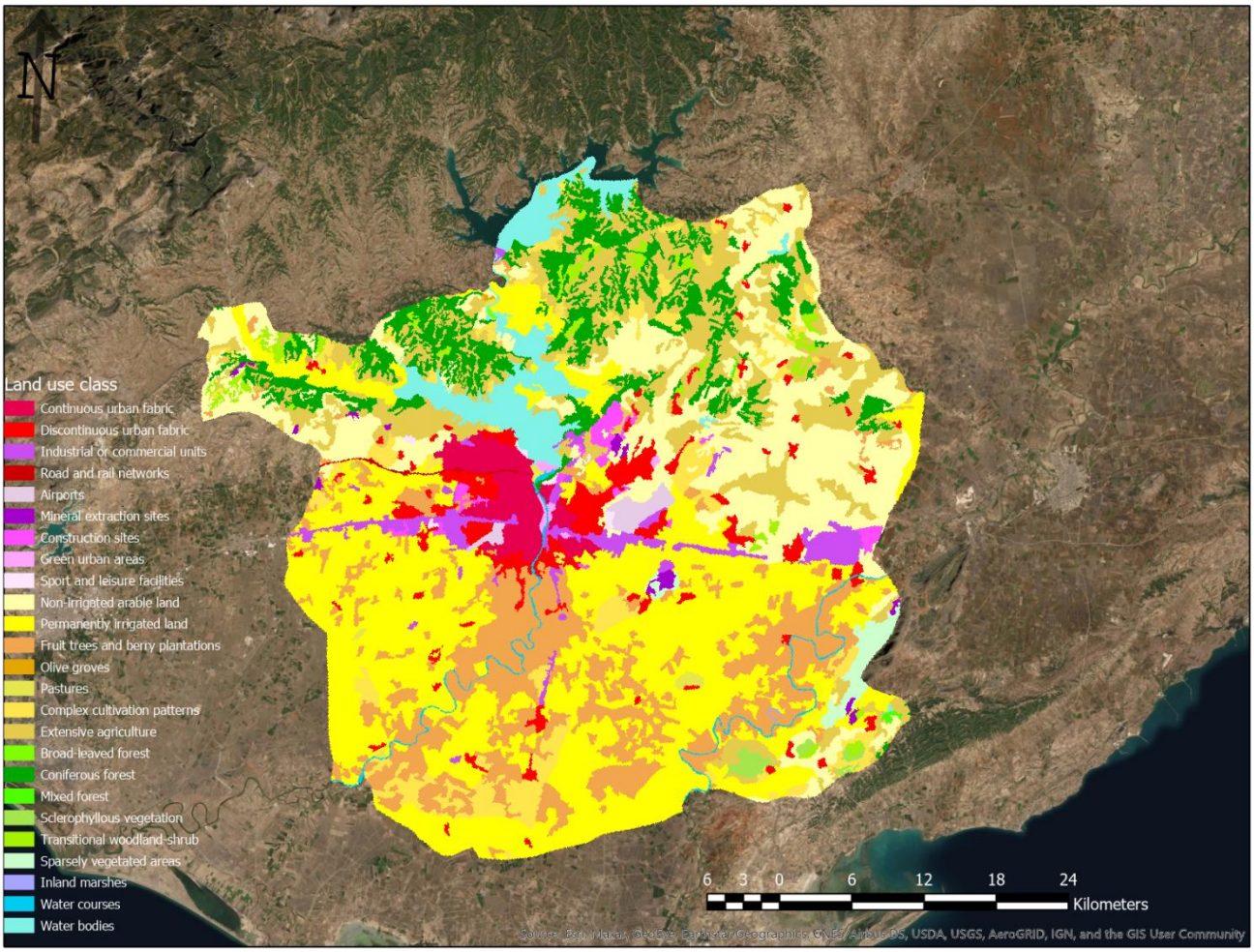

Figure 7. Land use classes in the study area, obtained from the Copernicus services.

3. Theory

In chapter 3.1 to 3.3, the processes and terminology behind the earthquakes, landslides and floods are explained to get an insight in how, when and why these natural hazards occur. In chapter 3.4 and 3.5, the concept of risk assessment is explained. Terminology, methodologies and constructs behind risk assessments are elucidated.

In contrast to the study area treated in this study, many studies have been conducted in data rich environments. Examples are the many studies in California, where earthquake research is extremely developed. Satellite imagery and sensors are dense here, which results in more possibilities for earthquake estimation and research (Elliott, 2020). The same accounts for landslides in the Alps. Inventories of landslides are present in abundance in these areas (Turcotte, et al., 2006). Also, data rich areas concerning flood hazard assessment profit from the abundance of inventory data. Probabilistic approaches using river runoff data or detailed precipitation peak data offer great methods to calculate flood hazard accurately. The Netherlands is a great example of a data rich area concerning water related data (Pfister, et al., 2004). It is a challenge to present an accurate and reliable results in a data scarce region, but, when achieved, it offers great opportunities for risk and hazard research globally.

3.1 Earthquakes

Earthquakes are defined as the shaking of crust resulting from a sudden energy flux in the lithosphere. Tectonic plates move, which causes friction between them. Tension builds as plates are stuck, which causes a massive energy release when a fault ruptures. A fault is a semi-planar system where rocks are displaced. When two plates are sliding against each other at a fault, rough edges might break off, releasing these sudden energy fluxes also known as fault ruptures. There are 3 main types of faults which have different impacts on the earth's surface. Strike-slip faults occur on transform boundaries (A), normal faults occur on divergent boundaries (B) and reverse faults occur on convergent boundaries (figure 8)

The seismic waves that are released from this rupture is what we call an earthquake. There are three types of seismic waves; P waves, or primary waves, travel through the earth's crust at six kilometer per second and are the fastest waves out of the three, S waves, or secondary waves, can only travel through solid materials and reach a speed of three kilometer per second. The movement of the S wave is similar to whipping a rope back and forth. When P and S waves reach the earth's surface, Love waves

are formed. The Love wave is a surface type wave and cracks building foundations, walls and infrastructure easily due to its complex vertical and horizontal movement (Keller & DeVecchio, 2015).

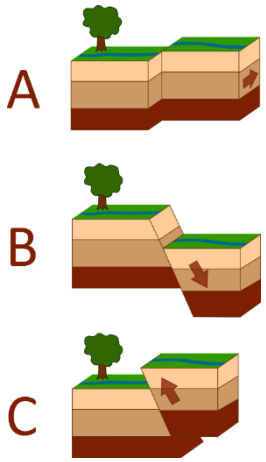

Figure 8. The 3 main types of faults. A = Strike-slip fault, B = Normal fault and C = Reverse fault the 1998 Adana earthquake was a typical strike-slip earthquake (Kuru & Ulusay, 2004).

The focus of an earthquake is the location in the crust where the fault was ruptured. Seismic waves lose their energy, referred to as attenuation, when traveling upwards through the crust and are therefore less strong, decreasing their potential damage. The 1998 Adana earthquake had a focus depth of 23 km (Kuru & Ulusay, 2004), which is classified as a shallow-focus earthquake (Spence, 1977). Another factor that influences the amount of shaking, and therefore potential damage, is the local geological conditions. Material amplification, or the change in level of shaking due to the change in surface material, strongly influences the amount of ground motion. The level of shaking increases with the level of water-saturation (table 2).

Table 2. When shear wave velocity slows down, the horizontal motion is transferred to vertical motion, which increases shaking. Shear wave velocity and shear strength decrease with the level of water content in a soil (Bauer, Kiefer, & Hester, 2001).

Soil type NEHRP	General description	Average shear wave velocity (m/s)	Average blow counts	Average shear strength (kPA)
A	Hard rock	> 1500		
B	Rock	760–1500		
C	Hard and/or stiff/very stiff soils; most gravels	360–760	> 50	> 2000
D	Sands, silts and/or stiff/very stiff clays, some gravels	180–360	15–50	50–100
E	Small to moderate thickness (10–50 ft) soft to medium stiff clay, plasticity index > 20, water content > 40%	< 180	< 15	< 50
E_2	Large thickness (50–120 ft) soft to medium stiff clay plasticity index > 20, water content > 40%	< 180	< 15	< 50

When shaken, pore water pressure increases until bearing strength is lost, which causes liquefaction. A near-surface layer of water-saturated sand changes quickly from solid to liquid, which is common with earthquakes of M_s 5.5 and above where the soil is made up of Holocene sediments (Dokka, 2006). An indicator of liquefaction are sand boils or sand volcanoes, which are formed as a result of increased pressure on the saturated sand layer deep in the ground. This causes the sand to rise through the layers above and erupt above the surface (Keller & DeVecchio, 2015) which was typically seen during the 1998 Adana earthquake (Kuru & Ulusay, 2004). Liquefaction is known to cause great damages to building foundations.

One particular physical characteristic of the study area that plays an important role in defining earthquake hazard in a deterministic way is soil. Not only does soil play an important role in the calculation of peak ground acceleration (Ulusay, et al., 2004), but also in defining the severeness of soil liquefaction (Seed & Idriss, 1969). Earthquakes are known to cause a chain reaction with other hazards. Examples are ground rupture, land subsidence, landslides, fires and diseases (Keller & DeVecchio, 2015).

3.2 Landslides

A landslide, or mass wasting, is any type of downslope movement as a coherent mass under the main influence of gravity. Different types of landslides result in different consequences for soil in both upslope and downslope area. The type of landslide is distinguished on four variables: 1) Type of movement (slide, fall, slump, flow or creep), 2) Type of moving material (rock, soft sediments, etc.), 3) Amount of water present and 4) Velocity.

A landslide occurs when a slope becomes unstable. The stability of a slope can be evaluated by looking at the relation between resisting forces, which favor the stability of a slope, and driving forces, which favor a downward movement of materials (Keller & DeVecchio, 2015). This relationship is described by the Factor of Safety (FoS) (equation 1).

Equation 1.

$$FoS = \frac{resisting\ forces}{driving\ forces}$$

Where the most common driving force is the weight of the material added to objects located on top of the material, examples of the latter are buildings and vegetation (Schwarz, et al., 2010). The resisting force is the resistance to sliding, falling or flowing of the earth materials located on the slope. If the FoS is greater than 1, the slope is considered to be in a stable situation. If the FoS is less than 1, the slope is considered to be in an unstable situation (de Vugt, 2018). Resisting forces and driving forces change over time due to the environment being dynamic (Sivrikaya, et al., 2008). Changes in stresses

can be induced by earthquakes, changes in earth materials, human made structures or, the most common trigger, by pore pressure changes due to heavy rainfall. When pore water pressure increases, the shear strength of the soil, also known as the resisting force in the FoS, decreases, lowering the FoS (Sidle & Swanston, 1982). There are many parameters that influence landslide occurrence. Most of these relate to soil conditions. Examples are soil cohesion, weight, thickness and effective angle. Also, the digital elevation model plays a large role in the calculation of land slide hazard (Brunsden & Prior, 1984).

Landslide inventories are a crucial part of any probabilistic approach of landslide susceptibility mapping (Pardeshi, et al., 2013). A landslide inventory would also be of use for validation purposes with a deterministic approach, but the quality of the result is not as dependent on data as with the probabilistic approach. To get the best result as possible with the data that is available in the area, a deterministic and heuristic approach will be applied.

3.3 Floods

Rivers provide water for industry and agriculture and enable ways of transport, which is why people generally always lived close to rivers. Living on riverbanks involves high risk, since flooding is one of the most dangerous natural hazards (Crunch, 2008) affecting the most people yearly out of all natural hazards (Ritchie & Roser, 2019).

Flooding is the natural process of overbank flow. These can be characterized in different ways, including the discharge or stage of the river at the moment when the flooding occurs. The amount of flooding does however not immediately translate into damages, since several factors need to be looked at before assessing potential damages. Examples are land use, duration of flooding, time of year, quantity and type of sediment transported and deposited by the flood and the level of forecasting and evacuation.

Climate plays a crucial role in the distribution of runoff over the course of a hydrological year. In the northern hemisphere, winter thickens the snowpack in mountainous areas and saturates the soil in the zone of transport. This causes the surrounding areas to be extra prone to river floods during spring since river runoff will be higher. Especially in Mediterranean climates, rare flooding events with recurrence intervals of over 50 years shape the fluvial system (Inbar, 2020). These flash floods, which are typically produced by intense rainfall of short duration over a small area, cause the peak discharge to be reached in a matter of minutes. Although flash floods are very local, they can cause problems in downstream areas where they join and cause great damage to arable lands and urban environments (Keller & DeVecchio, 2015).

As with landslides, a flood inventory is not available in this area. Therefore, the same combination of deterministic and heuristic is applied. A few characteristics of the study area that play a big role in the deterministic calculation of flood hazard is the level of infiltration, the elevation and rainfall intensity (Kourgialas & Karatzas, 2011).

3.4 Risk assessment

Several concepts need to be distinguished to define risk from natural hazard. Calculating the risk of an exposed element, a building for example, requires an assessment of the elements' vulnerability. Vulnerability expresses the proneness to damage of a particular element. Combining vulnerability with hazard, which is the potential damage an event can cause, translates to risk. Therefore, to assess risk from a certain natural hazard, both hazard and vulnerability need to be identified and evaluated separately first (van Westen, et al., 2006) (Douglas, 2007). The level of natural hazard is based purely on environmental parameters, triggering factors and the reoccurrence interval of the specific event. Geology, soil, land use, slope, rainfall, seismicity and other factors influence the potential damage an event can cause. The level of vulnerability is determined by elements at risk, such as population, buildings and infrastructure (figure 9).

While defining hazard, it is important to relate it to the level of potential damage the hazard can cause. The level of earthquake hazard can be defined by several magnitude scales. The surface magnitude scale (M_s) is based on either the Rayleigh waves or Love waves produced by the earthquake. The higher the magnitude, the more potential damage an earthquake can cause. Vulnerability is not included in this scale (Havskov & Ottemöller, 2010). An earthquake with an M_s of 6.0 in San Francisco will most likely cause more damage than an earthquake with an M_s of 9.0 in Alaska. For floods, flood water height or river discharge is used. For landslides, depending on the mapping method, depth of failure plain, volume of failed material, debris flow depth/speed or FoS is used (de Vugt, 2018).

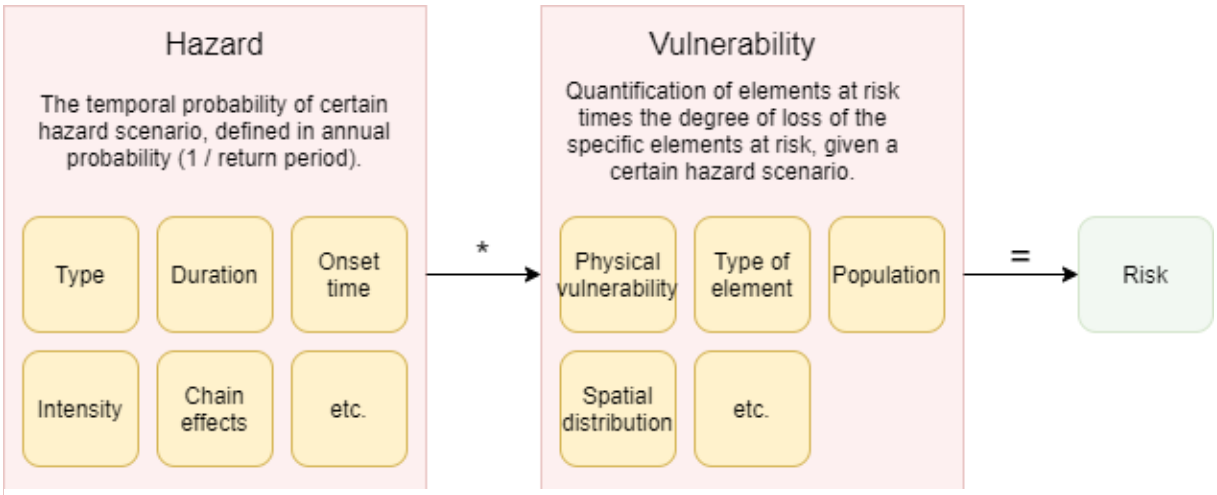

Figure 9. The concepts of hazard, vulnerability and risk explained.

Social vulnerability combines both the proneness of a population to a certain natural hazard and the ability to respond to and recover from the impacts. Proneness of a population can be calculated by making use of an inventory of elements at risk. The second part of social vulnerability is however harder to measure. Examples of characteristics that can be taken into account are age, income and race. These factors can influence unwillingness to cooperate with mandatory evacuation orders or their physical/economic inability to do so. Data quality and access make it however hard to capture this and limit the development of measurements of social vulnerability (Cutter & Finch, 2008).

3.5 Multi hazard risk assessment

Multi hazard mapping is crucial for governments and city planners to reduce losses from disasters. The importance of reducing these losses pre-disaster instead of post-disaster is getting more awareness in vulnerable regions. Hazard prevention, property and natural resource protection, public education and emergency services need multi hazard risk assessments in order to be applied accordingly (Tate & Cutter, 2010). In order to assess the combined natural hazard risk, the hazard types and their processes need to be assessed separately on their risk first. To do this, different methods need to be used. A methodology that works for one hazard type might not be suited for another (Bostançı, et al., 2017).

The quantitative method is the preferred type of analysis as this results in more tangible results and can therefore be compared with results from similar studies in other areas. Also, updating the model input is easier when compared to a quantitative method, making the model more flexible. It is however true that qualitative methods are better suited for small scale studies and are less data dependent (Dai, et al., 2002). When data is scarce on a specific subject, the qualitative approach may be more favorable than the quantitative approach. Since both approaches have their advantages and disadvantages, the fitness of either one of these methods depends on the data availability and could differ between the three hazard types in this research.

A major issue in multi hazard risk assessments is the many different types of methods, which leads to problems when comparing the results of different studies in calculating both hazard and vulnerability. Two approaches can be distinguished, a spatially oriented approach and a thematically defined approach. The spatially oriented approach tries to aggregate all hazards and associated vulnerabilities in the area, while the thematically defined approach tries to include the influence and interaction of one hazard with another. This means that the process of chain reactions or cascades are included in the approach, which is more complicated to assess, but generally gives a more realistic view of the situation (Kappes, et al., 2012). However, these cascades are often very area-specific, which causes cases in different parts of the world often to be incomparable (Oberndofer, et al., 2020). The choice of which approach to use is fully dependent on the aim of the study and the used spatial and temporal

scales (Fuchs & Thaler, 2018). Since this study combines flood hazard, earthquake hazard and landslide hazard, there is most definite overlap present between the approaches of the different hazards. Both flood triggers and earthquake triggers influence the spatial distribution of landslide hazard. However, to use the cascade methodology to an extent as in the papers above requires very specific data which is unavailable for this study area. A simplistic version of the cascade method will be applied, where overlap between the hazards is noticeable.

Deterministic approaches do not include elements of randomness. Most multi-hazard assessment studies are based on a deterministic model, where the probability of a hazard is multiplied by the expected consequences (Varnes, 1984). In contrast to the deterministic approach, the probabilistic approach is underrepresented in scientific studies. However, this approach does offer realism since it is based on randomness. The values and input parameters are described with probability distribution functions, since totally certain input parameters are unavailable due to lack of data (Kirchsteiger, 1999). While deterministic methods display results as a single sharp number where vulnerability and risk are unavailable to be noticed separately, the probabilistic method displays the results using probability distribution functions, where both risk and vulnerability are more easily interpretable (Oberndofer, et al., 2020). Since the study area is very data poor, a combination between probabilistic approach and a deterministic approach could offer a solution. Probabilistic approaches will play a bigger role in defining frequency magnitude relations by applying probability distribution functions, while the deterministic approach will be crucial in defining the end result of the specific hazards and combining them with vulnerability to obtain risk.

3.6 Conclusion

In this region, spatial data and meteorological data is very scarce or inaccessible. Therefore, global and open-source data need to be utilized as best as possible.

The greatest challenge is relying solely on triggering factors to calculate flood and landslide hazards, since inventories for both hazards are inaccessible or unavailable and deterministic, high quality methods concerning both hazard types are scarce. Frequency – magnitude relations will still be calculated, compared and, in combination with other indicators, translated into hazard. Since the amount of available data differs per hazard, different approaches will be used. This will cause friction, since aggregating, overlaying and comparing the results will be more difficult. However, such a heuristic approach is necessary to approach each hazard accordingly while still being able to combine these to a multi hazard assessment. For all hazards, Esri's ArcGIS software will be used to conduct a spatial analysis of the gathered data. Raster calculator helps overlaying the different datasets and points are easily converted to rasters with interpolation techniques such as kriging or IDW. Excel will

help translating inventories into frequency - magnitude relationships, which can be inserted into ArcGIS. The main output will be in map format, demonstrating hazard, vulnerability and hazard of all three hazard types. An elaboration of the methodology will be demonstrated in chapter four.

4. Methodology and data

The methodology of this research consists of 4 separable parts. Respectively, these are pixel-based calculations of earthquake hazard, flood hazard, landslide hazard and calculating risk. The order in which these calculations are done are not random. Landslide hazard is, among other parameters, dependent on the wetness of the surface and earthquake occurrence (Brunsden & Prior, 1984). In order to execute these calculations accurately, it is practical to do the earthquake and flood calculations first. Risk is then obtained by determining the value of the land use classes. Adding damage functions, which differ for each type of hazard, results in damage maps for each hazard type. The fact that the value map can be used to calculate risk for each type of hazard makes this methodology very efficient and makes the results comparable to other hazard types. Figure 10 portrays a flowchart of the complete process conducted in this research.

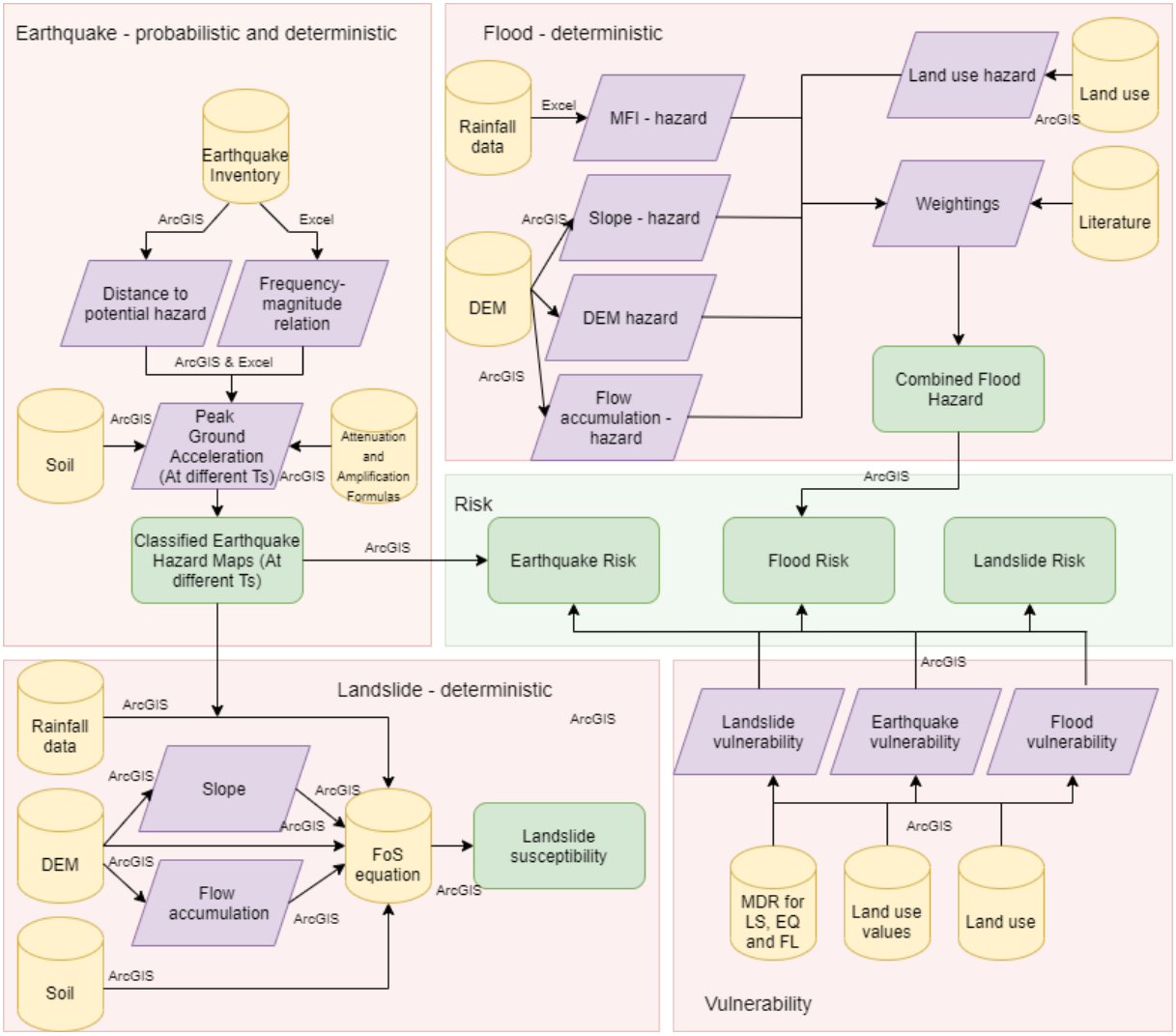

Figure 10. Flowchart of the complete study.

4.1 Earthquake hazard

Earthquake hazard is calculated by making use of a combination of probabilistic and deterministic methodologies. In the probabilistic part the recurrence interval and the frequency magnitude relation are calculated. The recurrence interval is needed for the deterministic part of the analysis, where magnitude is a key parameter in the PGA (peak ground acceleration) equation.

4.1.1 Calculation

Peak ground acceleration (PGA) is a unit used in many different studies when calculating earthquake hazards (Irwansyah, et al., 2013) (Schenk, et al., 2000) (Ram & Guoxin, 2013), and is because of its success also used in this study. PGA can be calculated by making use of the attenuation formula, which occurs in many different forms in earthquake literature (Fukushima & Tanaka, 1990) (Boore, 1987) (Campbell, 1981). In this research, the attenuation relation of Ulusay et al. (equation 2) (Ulusay, et al., 2004) is used, because it is specifically drafted for the Anatolian plate and because of its inclusion of the hypocentral distance instead of the epicentral distance.

Equation 2.

$$PGA = 2.18e^{0.0218(33.3M-R+7.8427S_A+18.9282S_B)}$$

Where PGA is calculated in gal, M is the magnitude and R is the hypocentral distance in kilometers. S_A and S_B are soil parameters, where S_A and S_B are equal to zero for rock sites, S_A is one and S_B is zero for medium to hard soil sites and S_A is zero and S_B is one for soft soil sites.

To optimally describe the PGA in this area, different scenarios for M are drafted. These scenarios are based on the frequency-magnitude relation, which has always been a reliable source for earthquake forecasting (Nishenko, 1985). The frequency-magnitude relation differs per location and can be calculated by making use of an earthquake inventory describing historical events (figure 11). The Gutenberg-Richter relation (equation 3), which is often used when no earthquake inventory is available (Gutenberg & Richter, 1944), can be used to validate the results of the frequency-magnitude relation.

Equation 3.

$$\log n = a - bM$$

Where n is the number of events, M is the magnitude and a and b are location-dependent constants. For the Anatolian plate, a and b are found to be 4.8 and 0.9 respectively (Kalyoncuoglu, 2007).

4.1.2 Parameters and data

Except for the magnitude scenarios, the input for the calculation needs to be in raster format. For the magnitude scenarios an earthquake inventory, including time of earthquake and magnitude of earthquake, is needed. This inventory is obtained from the USGS earthquake catalog (USGS, 2020). For

the PGA equation, parameters S_A and S_B are based on the soil grids of IRSRIC (ISRIC, 2020) (figure 5). Furthermore, earthquake depth and earthquake location are needed, which are also obtained from the earthquake inventory.

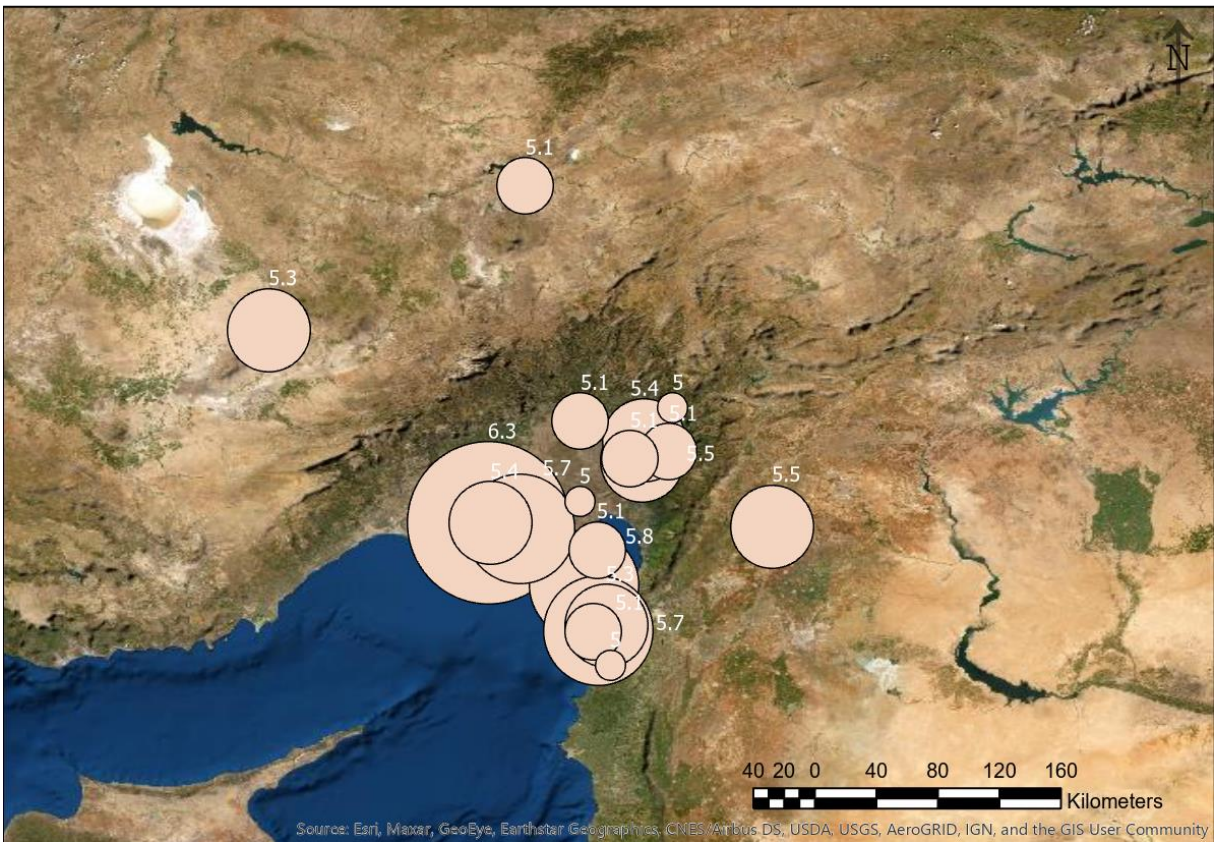

Figure 11. Historical earthquake events in the study area (USGS, 2020).

4.2 Flood hazard

Flood hazard is calculated using a deterministic method. Even though discharge data of the Ceyhan river is available through the Global Runoff Database (GRDC), most floods in the Adana area are flash flood related (Seçkin & Topçu, 2016). Furthermore, the most defining river in the area is the Seyhan river, not the Ceyhan river. Thirdly, discharge data only runs until 1980, which makes the dataset inaccurate for present times. A deterministic method for calculating flash floods is the logical solution.

4.2.1 Calculation

The calculation is based on five different parameters, of which each have their own weighting. These weightings are according to the significance of the relationship these parameters have with each other, which is a method developed by (Shaban, et al., 2001). The parameters are elevation, flow accumulation, rainfall intensity, land use and slope. In the original methodology, geology is also considered. However, there is no dataset of parent material of the area available. Therefore, this

parameter is left out of the calculation. A schematic overview of the interaction between parameters is given in figure 12 (Kourgialas & Karatzas, 2011).

Major and minor effects are distinguished. The weights are quantified by assigning points to the arrows. A major effect contributes one point, and a minor effect contributes half a point. These result in the following weightings: Elevation 3.5 points, rainfall intensity 1.5 points, land use 2.5 points, flow accumulation 1.5 points and slope 2 points.

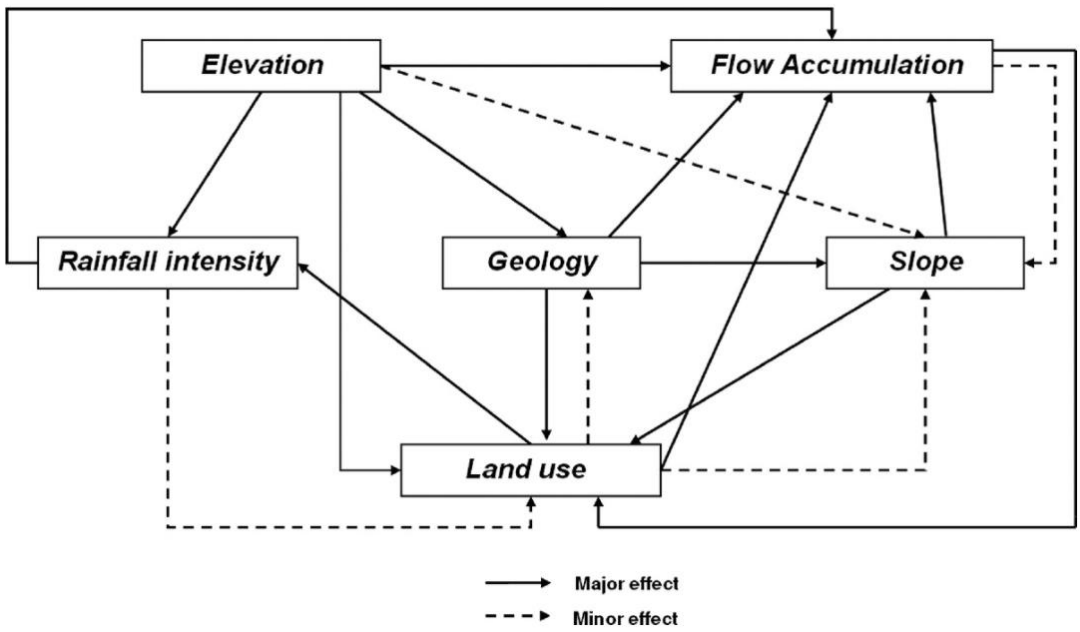

Figure 12. A schematic overview of the interaction between all involved parameters according to Kourgialas & Karatzas (2011). In this study, geology is left out since no reliable data source for parent material is available.

4.2.2 Parameters and data

The parameters are viewed in raster maps across the Adana area. The original rasters are displayed as a stretch of the value. To apply the weightings and draw borders between different hazard levels, the display method is changed from stretch to five classes, which are based on the Jenk's Natural Breaks method (Smith R. , 1986). These classes are assigned hazard levels and ratings: Very high (=10), High (=8), Moderate (=5), Low (=2) and Very Low (=1) (table 3).

The slope and flow accumulation rasters are obtained from the ASTER global digital elevation model (DEM) (ASTER, 2020). By applying the slope tool on the DEM, the steepness of each cell can be identified in degrees (equation 4).

Equation 4.

$$tan\theta = \frac{rise}{run}$$

Where θ is the degree of slope. By applying the flow accumulation tool, the accumulated weight of all cells flowing into each downslope cell is calculated. Flow accumulation is based on flow direction, which is based on the DEM (figure 13). The weight raster of flow accumulation is set to one since rainfall intensity is considered separately.

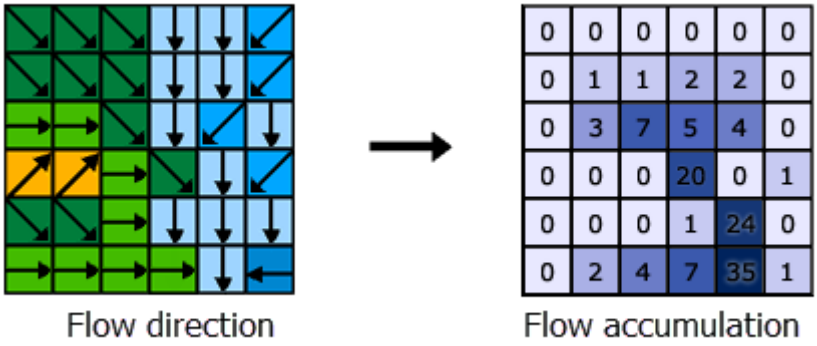

Figure 13. Flow accumulation is based on flow direction. The tool counts how many cells are flowing into each downslope cell (ESRI, 2020)

Table 3. Values and corresponding level of hazard, rates and weights for the different parameters, based on the study by Kourgialas & Karatzas (2011).

Parameter	Value	Level of hazard	Rate	Weight
Elevation	0 – 58m	Very high	10	3.5
	58 – 135m	High	8	
	135 – 213m	Moderate	5	
	213 – 366m	Low	2	
	366 – 766m	Very low	1	
Land use	Disc. urban	Very high	10	2.5
	Continuous urban	High	8	
	Arable land	Moderate	5	
	Forest	Low	2	
	Water bodies	Very low	1	
Rainfall intensity	122 – 128mm	Very high	10	1.5
	117 – 122mm	High	8	
	112 – 117mm	Moderate	5	
	109 – 112mm	Low	2	
	0 – 109mm	Very low	1	

Slope	0 – 3 degrees	Very high	10	2
	3 – 7 degrees	High	8	
	7 – 12 degrees	Moderate	5	
	12 – 22 degrees	Low	2	
	22 – 71 degrees	Very low	1	
Flow accumulation	2199 – 6245 cells	Very high	10	1.5
	818 – 2199 cells	High	8	
	317 – 818 cells	Moderate	5	
	78 – 317 cells	Low	2	
	0 – 78 cells	Very low	1	

The Modified Fournier Index (MFI) method (equation 5) can be used to calculate precipitation peaks in a dataset of means (Morgan, 2005). Rainfall intensity can therefore be obtained from a dataset of monthly averages. These monthly averages are gathered from the Turkey State Meteorological Service (MGM) for twelve different weather stations in the Adana province.

Equation 5.

$$MFI = \sum_{1}^{12} \frac{p^2}{P}$$

Where Σ_1^{12} is the twelve-month summation, p is the average monthly rainfall and P is the average annual rainfall. To interpolate the MFI values of the twelve weather stations, the kriging interpolation method is used since this is optimal when spatial association is present (Attorre, et al., 2007). The Kriging tool weights the surrounding measured values to obtain a prediction for an unmeasured location (equation 6).

Equation 6.

$$Z(S_0) = \sum_{i=1}^{N} \lambda_i Z(S_i)$$

Where $Z(S_i)$ is the measured value at the *i*th location, λ is the weight of a measured value, s_0 is the to be predicted location and N is the number of measured values.

The land use dataset, obtained from Copernicus Land Monitoring Service, is also reclassified into five classes. These classes are based on their Curve Number (CN) values.

4.3 Landslide hazard

Landslide hazard is calculated by making use of a deterministic method, since no landslide inventory is available. Landslide hazard makes use of the Fournier index, which is also used in the flood hazard calculation, and the PGA of a 50-year earthquake. This calculation is therefore dependent on the previous two hazard calculations.

4.3.1 Calculation

The deterministic pixel-based landslide calculation is based on an equation by Brunsden and Prior (Brunsden & Prior, 1984). Without looking at any cascade reactions, the formula is equal to equation 7.

Equation 7.

$$FoS = \frac{c' + (\gamma - m\gamma_w)zcos^2\beta tan\Phi'}{\gamma z sin\beta cos\beta}$$

Where FoS is the factor of safety, c' is the effective cohesion in Pascal, γ is the unit weight of soil in Newton per cubic meter, γ_w is the unit weight of water in Newton per cubic meter, z is the depth of failure surface in meter, z_w is the depth of the water table in meter, m is the ratio z_w/z, β is the slope surface inclination in degrees and Φ is the effective angle of shearing resistance in degrees.

According to multiple studies, earthquakes and heavy rainfall are triggering factors in landslide occurrences (Gorum, et al., 2011) (Harp & Jibson, 1996) (Chang, et al., 2007) (Terlien, 1998). According to Brunsden and Prior, the earthquake triggering factor can be included in the FoS equation (equation 8) (Brunsden & Prior, 1984).

Equation 8.

$$FoS = \frac{c' + z(\gamma cos^2\beta - \rho\alpha_h N cos\beta sin\beta - \gamma_w m cos^2\beta)tan\Phi'}{z(\gamma sin\beta cos\beta + \rho\alpha_h N cos^2\beta)}$$

Where ρ is the soil weight in kilograms per cubic meter, α_h is the PGA in meter per second squared and N is the amplification (table 4). PGA is retrieved from the earthquake calculation and transferred from gal to ms^{-2}. P is calculated by translating γ from N m^{-3} to kg m^{-3}.

4.3.2 Parameters and data

The values for the parameters are mostly dependent on soil group type. In this study area, three types of soils can be distinguished: Vertisols, Luvisols and Leptosols (figure 5). In table 4, the values for the soil-related parameters are given. Again, soil parameters are based on the soil grids of ISRIC (ISRIC, 2020).

Table 4. Parameter values for the different soil groups present in the area for effective soil cohesion (c'), unit weight of soil (γ), effective angle of shearing resistance (Φ) and amplification (N) (Semblat, et al., 2005) (Swiss Standard) (Encyclopaedia Brittanica, 2016) .

Parameter	Luvisol	Leptosol	Vertisol
c’	10.000 Pa	0 Pa	13.000 Pa
γ	17.000 N m^{-3}	15.300 N m^{-3}	19.370 N m^{-3}
Φ	35°	23°	50°
N	1	0.55	1.3

Just as in the flood hazard calculation, slope inclination is calculated by applying equation 4 on the obtained digital elevation model. The depth of the soil is obtained from NASA’s Earthdata, which provides a global one kilometer gridded thickness of soil cover (NASA , 2020). To calculate m, the height of the water table is also needed. This dataset is however unavailable for the study area. To accurately mimic water table height distribution, m is calculated by making use of the Fournier Index (equation 5). By using the output raster of the Fournier index as input weight for flow accumulation, the amount of water present in each cell can be calculated. This value, normalized between zero and one, is used as the level of saturation (m).

4.4 Risk

To effectively reduce damages induced by natural hazards, decision makers require an in depth understanding of natural hazard risk. Many regions dealing with severe natural hazard risk lack financial resources, only adding pressure to the process of minimalizing cost (Alcántara-Ayala, 2002). Reliable estimates of potential damages resulting from earthquakes, floods and landslides in the Adana area are crucial for decision making, land use planning and policy making.

Risk can be expressed in five types of costs: Direct costs, business interruption costs, indirect costs, intangible costs and risk mitigation costs. To accurately estimate all five types of costs, a substantial amount of accurate data is required, which is simply not present in the study area. To simplify the process and still get an accurate estimation of risk, only direct costs are considered in this study. Direct costs are defined as damages to property due to direct physical contact with hazard (Smith & Ward, 1998).

Since cascade reactions are already considered in the hazard calculation, risk is estimated by making use of a susceptibility function based on a single parameter.

4.4.1 Earthquake risk

Studies estimating earthquake risk are often based on a combination of building inventories, satellite images and population distributions (Ghasemi, et al., 2020) (Hashemi & Alesheikh, 2011) (Gunturi, 1993). In this study however, vulnerability of pixels is estimated by utilizing land use data. Since building inventories, population distributions and the time to train satellite images is not available, land use data offers a simple but accurate solution to estimate vulnerability of the area.

To estimate vulnerability, damage functions are used. These functions are based on empirical analyses in different areas under different conditions. Damage functions differ mostly based on building type and are expressed in mean damage ratio (MDR), which is the ratio of repairing costs over replacement costs (equation 9) (Wahlström, et al., 2004) (Ang & Tang, 1975).

Equation 9.

$$MDR = \Phi\left(\frac{\ln(PGA - \lambda)}{\zeta}\right)$$

Where Φ is a standard normal distribution function characterized by the average, λ, and the standard deviation, ζ. These parameters differ severely per building type and building date (Miyakoshi, et al., 1997). Most of the residential and commercial buildings in the Adana area were built during the last decades and are made of reinforced concrete frames with masonry infill walls (Wenk, et al., 1998). Since building inventories are incomplete, damage functions must be extracted from studies conducted in similar areas. A study by Askan and Yucemen estimated damage functions for several building types in the Turkish cities of Erzincan, Dinar and Duzce (Askan & Yucemen, 2010). Similar to the Adana area, earthquakes struck in these areas during the nineties. Of these three areas, Erzincan's damage function characteristics mimics Adana's damage function best, since Erzincan is on the same fault as Adana and both areas have similar building types (Wenk, et al., 1998) (Askan & Yucemen, 2010) (figure 14).

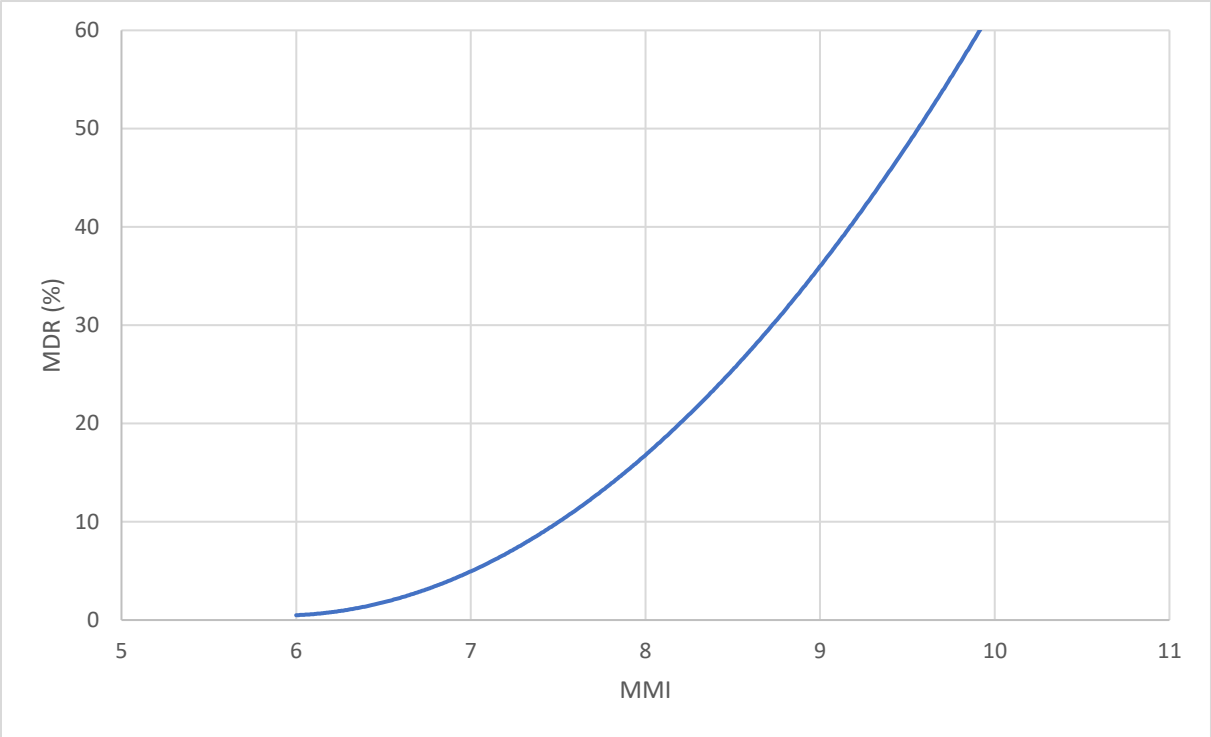

Figure 14. MDR function plotted against MMI for the Erzincan region (Askan & Yucemen, 2010).

Which results in the following MDR function (equation 10).

Equation 10.

$$MDR = 3.7 * MMI^2 - 43.5MMI + 128.5$$

Where MMI is the Modified Mercalli Intensity. Since the earthquake hazard calculation output in this study is expressed in PGA, a MMI to PGA conversion needs to be conducted. The relationship between MMI and PGA is very complex, since MMI is a subjective scale based on human response to ground shaking and damage observations (Linkimer, 2008) and PGA is objectively measured. Two different earthquakes with the same observed PGA can have different values for MMI depending on the characteristics mentioned in the sentence before. Different studies composed different relations between PGA and MMI, mostly depending on the region (Murphy & O'Brien, 1977) (Richter & Gutenberg, 1942) (Trifunac & Brady, 1975). The relationship constructed by Murphy & O'Brien is used in this study, since it is conducted in a Mediterranean region and its used for an MMI between IV and X (equation 11).

Equation 11.

$$MMI = 2.86 * \log(PGA) + 1.24$$

Since MDR is known, we only need to obtain a value for either the repair costs or replacement costs to estimate damages (equation 12).

Equation 12.

$$MDR = \frac{Repair\ costs}{Replacement\ costs}$$

Replacement costs are often replaced with market values of housing (Meroni, et al., 2017). To account for spatial differences in housing prices in the study area, a distinction is made between continuous and discontinuous urban area. Based on property prices by Numbeo, the price per square meter in the city center is 370 euros while outside of the city center the price drops to 250 euros (Numbeo, 2020). High-rise is not taken into account. Replacement costs of agricultural areas are obtained by using the market value of the area specific crops per hectare. Risk is then calculated by multiplying MDR with the replacement values.

4.4.2 Flood risk

Flood risk estimations are often based on satellite imagery of previous floods, rainfall data or river runoff data (Wheater, et al., 2005) (Benito, et al., 2004) (Youssef, et al., 2011). Flood hazard is calculated without using any runoff data, rainfall data or satellite imagery, since this data is unavailable. To translate the calculated flood hazard into risk, another method is used. Even though there are many methodologies to estimate flood risk, they all make use of damage functions to translate hazard into risk (Winter, et al., 2018) (Romali, 2019). A damage function is based on the object characteristics in an area and plots flood depth or duration against MDR (equation 12). Flood damage functions are already calculated for all continents by the Joint Research Centre (JRC) and are different per land use class (Huizinga, et al., 2017). For this study area, the Asian functions are chosen. The curves are smoothened since the accuracy reached by the JRC for Asia is not realistic for the Adana region. The different land use classes are weighted according to their presence in the study area and averaged to get one damage function for the entire study area (figure 15).

To calculate MDR, water depth is needed. The output of flood hazard is unitless but can be related to water depth. In the study by Kourgialas & Karatzas the output of flood hazard is validated against historical records. The severest floods in the past took place in the identified areas of high flood hazard (Kourgialas & Karatzas, 2011). The unitless output of flood hazard is fitted to an exponentially increasing water depth dataset from zero to five meters, to limit the number of pixels with high values. The five meters are chosen as a maximum based on expert judgement. This value will however not have a major effect on the output since the fitting is based on an exponential function (equation 13).

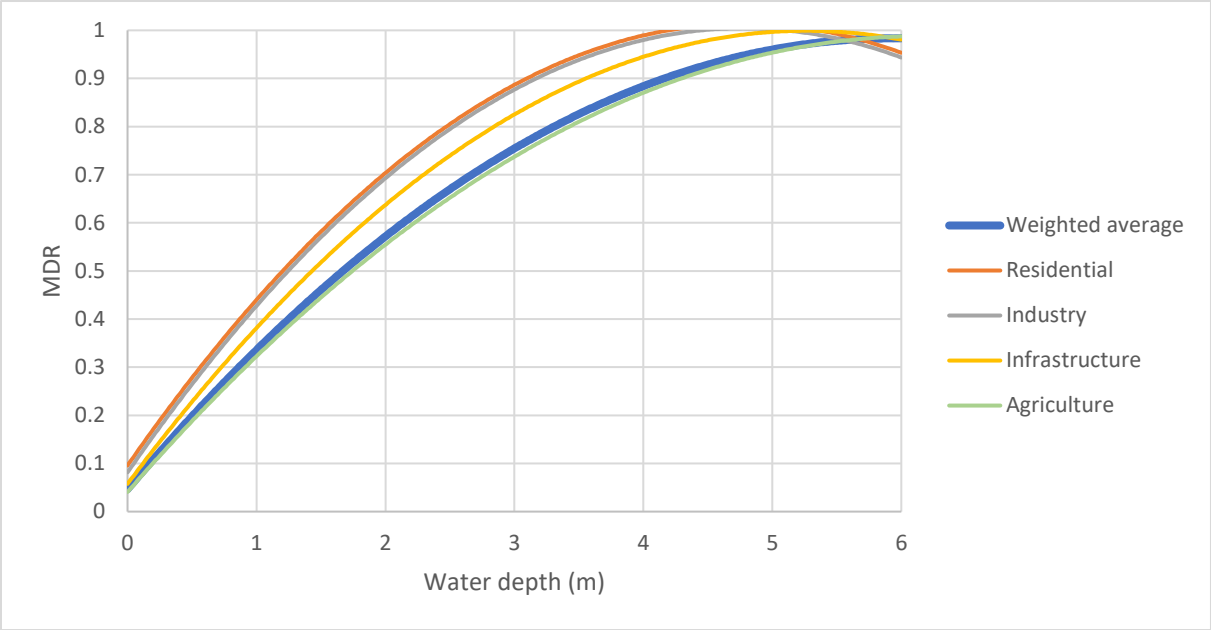

Figure 15. Flood depth-damage functions for Asia (Huizinga, de Moel, & Szewczyk, 2017). The weighted average is based on the pixel presence of each land use class.

Equation 13.

$$d = 5 * (\frac{S}{S_{max}})^3$$

Where d is the water depth in meters and S is the flood hazard. Then, the weighted average curve from figure 15 is used to calculate the MDR of each pixel (equation 14).

Equation 14.

$$MDR = -0.03d^2 + 0.32d + 0.05$$

As with the earthquake risk calculation, risk is then calculated by multiplying MDR with the replacement values.

4.4.3 Landslide risk

Similar to earthquake risk, landslide risk studies are severely dependent on building quality and building type data. A case study in Kuala Lumpur calculated the probability of a cell being occupied by an element at risk and combining this with spatial and temporal probability of a landslide occurring (Althuwaynee & Pradhan, 2016). This results in a very detailed and accurate risk assessment. There is however no data with the needed level of accuracy available for this study area. Another case study conducted in southern Italy focused on assessing landslide hazard while making use of very limited data concerning elements at risk. For every municipality, the monetary value of the elements at risk were defined and multiplied with calculated landslide hazard (Pellicani, et al., 2014). This results in very concrete monetary results, similar to the results of earthquake and flood risk of this study.

Monetary value of the area is calculated with land use data. The mean damage ratio formula based on the results from a study by Papathoma-Köhle et al., who constructed a damage curve based on landslide events investigated in different studies (equation 15) (Papathoma-Köhle, et al., 2015). (Fuchs, et al., 2007) (Totschnig, et al., 2011).

Equation 15.

$$MDR = 0.05m^2 + 0.15m$$

Where m is the intensity of the landslide. For an FoS < 0, m = 0. FoS translates directly to m between 0 and 3.22. Any FoS value above 3.22 results in an m of 3.22 since an m of 3.22 gives the maximum MDR value.

Similar to both earthquake risk and flood risk, MDR is multiplied with the value map to obtain landslide damages.

4.3 Data

The table below is constructed to display a complete and concrete overview of all used data and their purpose in this study. All data is referenced and their full citations can be found in chapter 8.

Table 5. Data used in this study. All data is referenced and citations can be found in chapter 8. EQ = Earthquake hazard, LS = Landslide hazard, FL = Flood hazard, RI = Risk calculation.

Name	Purpose	Source	Format
Earthquake Inventory	- EQ depth (EQ) - EQ magnitude (EQ) - EQ location (EQ) - EQ time (EQ)	USGS earthquake catalog	csv
Soil grids	- Attenuation parameters (S_A and S_B) (EQ) - FoS soil parameters (c', γ, Φ and N) (LS)	ISRIC SoilGrids	raster
Digital Elevation Model	- Elevation (FL) - Slope (FL, LS) - Flow accumulation (FL, LS)	ASTER	raster
Rainfall	- MFI (FL, LS)	Turkish Meteorological Institute (MGM)	point
Land Use	- Infiltration (FL) - Value of pixel (RI)	Copernicus Land Monitoring Service	raster

5. Results

The results of the hazard calculations of earthquake, flood and landslide hazard will be presented in this chapter. Afterwards, the risk calculation will be added to all three hazard types, presenting three maps of damages in the Adana area.

5.1 Earthquake hazard

Even though one of the two serves as input for the other, earthquake hazard calculation can be presented in two separatable parts: recurrence interval and PGA calculation. The recurrence interval is calculated and provides the following distribution (figure 16).

Table 6. Recurrence interval translated into Ts (recurrence intervals).

T	5	10	25	50	100
Magnitude	45	48	52	56	58

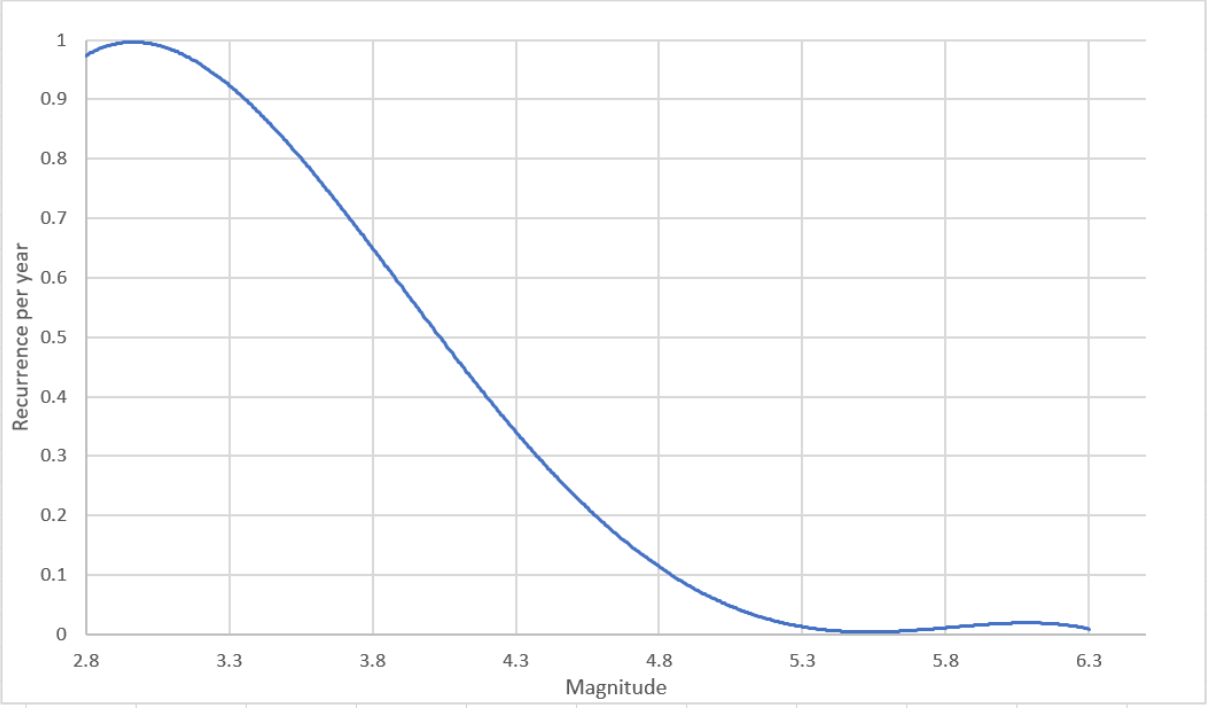

Figure 16. Earthquake recurrence interval in the study area.

The recognizable steep decline in recurrence interval is noticeable when increasing the magnitude. In this area, earthquakes with a magnitude larger than 6.0 are extremely rare. The Adana earthquake of 1998 was a one-in-a-hundred-year earthquake, which makes the scale of its destruction only more logical.

To construct the PGA maps, different scenarios are created. These scenarios are based on the values in table 6. They provide the following five maps (figure 17).

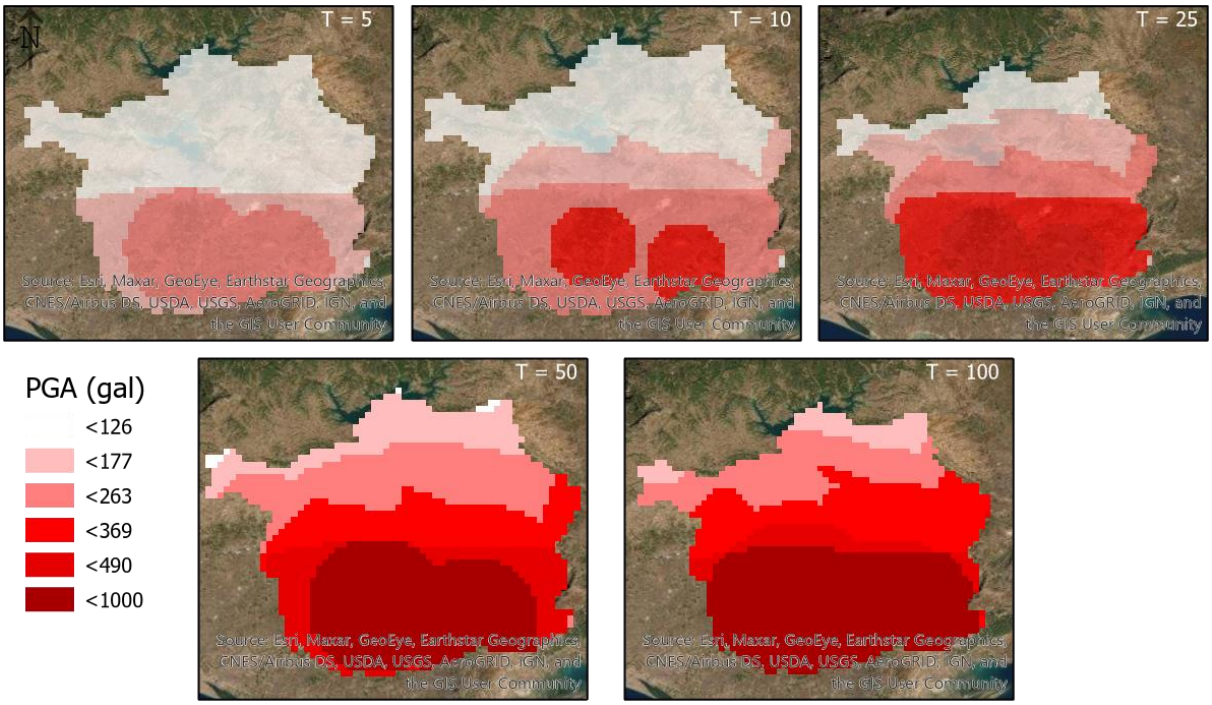

Figure 17. PGA value distributions over the study area for different Ts.

The southern part of the study area is dominated by high PGA values due to the softer soils and proximity to historic shallow earthquakes. Increasing the magnitude fades the circular buffer zones around these historic shallow earthquakes and creates a high to low pattern from south to north. PGA values of more than 200 gal are not noticeable in earthquakes with a T of five or lower. However, when doubling T from five to ten, PGA values go up to 350 gal in the south. The circular buffers around the historic heavy earthquakes are extremely noticeable in the T10 and T25 maps. Values of over a thousand gal are not reached every hundred years. Both T50 and T100 remain beneath this value. The difference between these two intervals is the extent of the dark area. In T100, the upper part of the estimated gal values extends over the whole southern part, while in T50 this is limited to the surroundings of the shallow historical earthquakes. A parallel can be drawn between the extend of the highest class of PGA values in T100 and the extend of vertisol soil in the area (figure 5).

The spatial distribution of both input variables is noticeable in the output. The circular buffers indicate the presence of shallow historical earthquakes while the south to north pattern indicates a soil distribution from soft soils to hard soils.

5.2 Flood hazard

Flood hazard is calculated by making use of five input parameters, each contributing to a final flood hazard map. Weightings are determined by the significance of influence the parameters have on each

other (table 3) (figure 12). To apply these weights, the original values of the parameters are transferred into rates of hazard (figure 18). After the transformation, applying a specific weight to each map results in the flood hazard map of the study area (figure 19).

Distribution of elevation in the study area dominates flow accumulation and slope patterns, and therefore accounts for a large part of the total hazard. The southern part of the study area is extremely flat, dominated by the thick vertisol soil profiles. The northern part, dominated by hard rock, has very steep slopes. Water therefore mainly flows southwards, accumulating on the vertisol plain. In the south east, a steep lone mountain range can be found resulting in the same process as in the north. Water flows from east to west accumulating on the vertisol plain. Based on this alone, the north is flood hazard free and the south would have trouble dealing with the accumulating water. These three variables account for seven out of the eleven weighting points of total flood hazard.

The other three weighting points are assigned to land use and rainfall. Land use has a very recognizable pattern of the city of Adana in the center of the study area, agricultural activities in the south and nature and green in the north. Infiltration values of urban area are extremely low, causing the highest hazard range to be in these land use classes. Green areas and agricultural areas offer more infiltration possibilities, resulting in low hazard in the north and south. Rainfall is distributed differently. Peaks are calculated with the MFI formula (equation 5), resulting in a high to low pattern form east to west. This variable accounts for only 1.5 points out of eleven.

The final map shows a combination of the patterns seen in figure 18. Some are more visible than others, depending on their weight. The steep and high north and south east contain little to no hazard, while the flat and fertile south contains most hazard. On the border of this transition from steep north to flat south, the city of Adana is located. Flood hazard is high here because of the high CN numbers. It is hard for water to infiltrate the ground in areas of discontinuous urban fabric. Peak precipitation increases slightly from east to west, influencing the final hazard map (figure 19)

5.3 Landslide hazard

Landslide hazard is calculated by making use of the factor of safety formula (equation 8). Input variables are slope and soil dependent, which can be noticed in the final hazard map (figure 20).

The steep slopes, which were also noticeable in the flood hazard map, can be seen in the north and eastern part, accounting for most of the unstable pixels. The effective angle, cohesion and soil weight is highest for the vertisols in the south. This depolarizes the overall image, creating unstable slopes in the south as well.

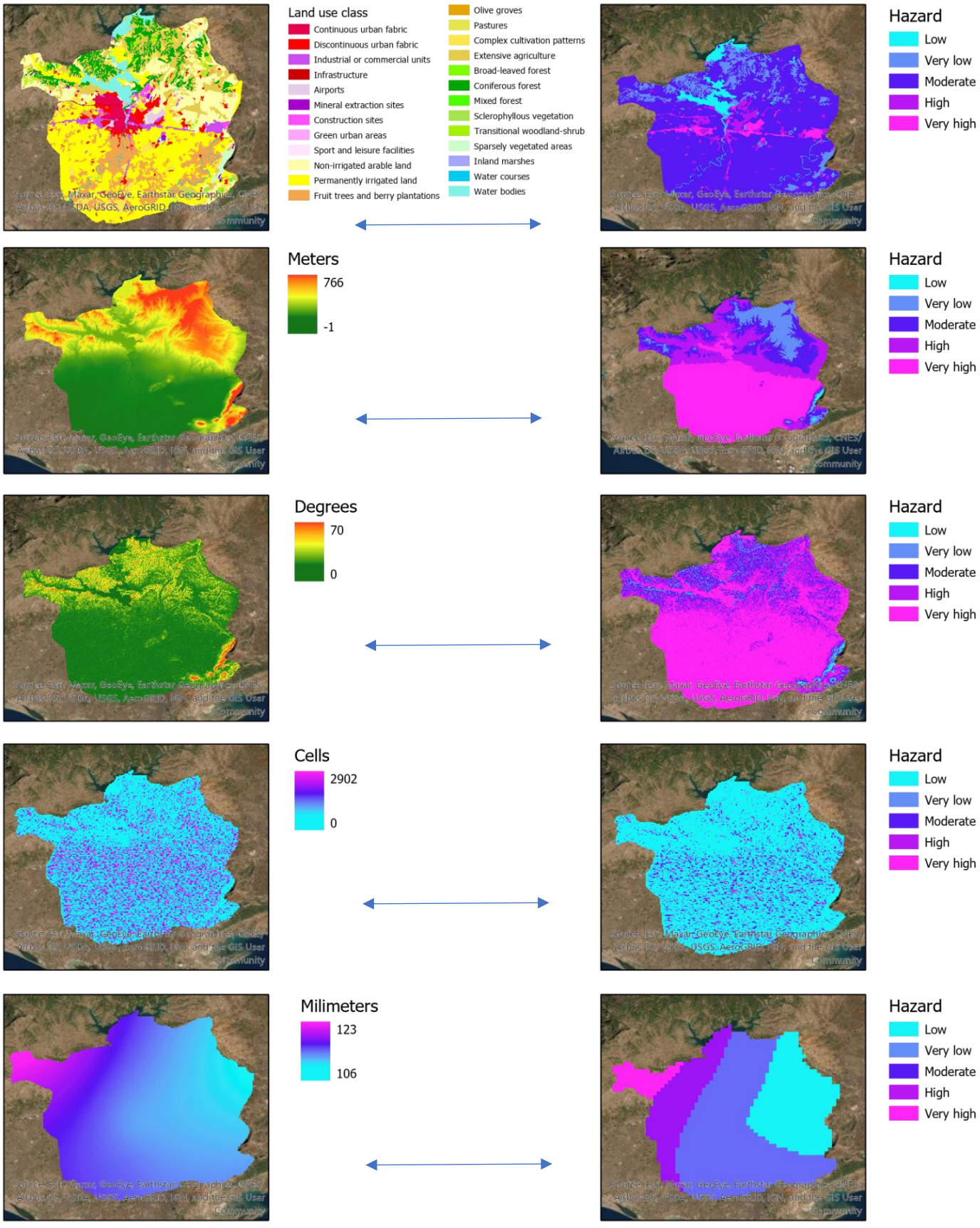

Figure 18. All input factors, consisting of land use, DEM, slope, flow accumulation and peak rainfall are translated into level of hazard using the rates of table 4.

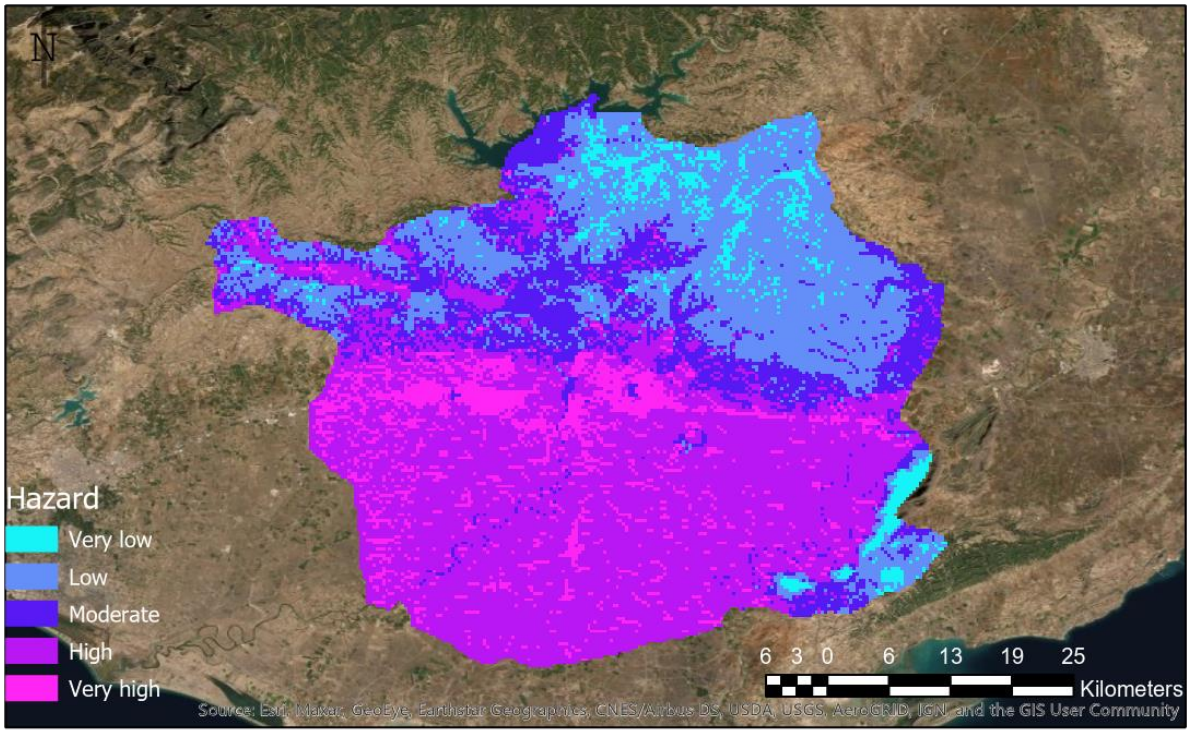

Figure 19. Overall flood hazard map configurated with ranks and weightings from table 3.

The city of Adana is however not recognizable in this map, since land use was not a parameter that was considered. It is remarkable that beneath the city unstable slopes are present in abundance. Assuming the municipality took precautions when building, these slopes are however safe.

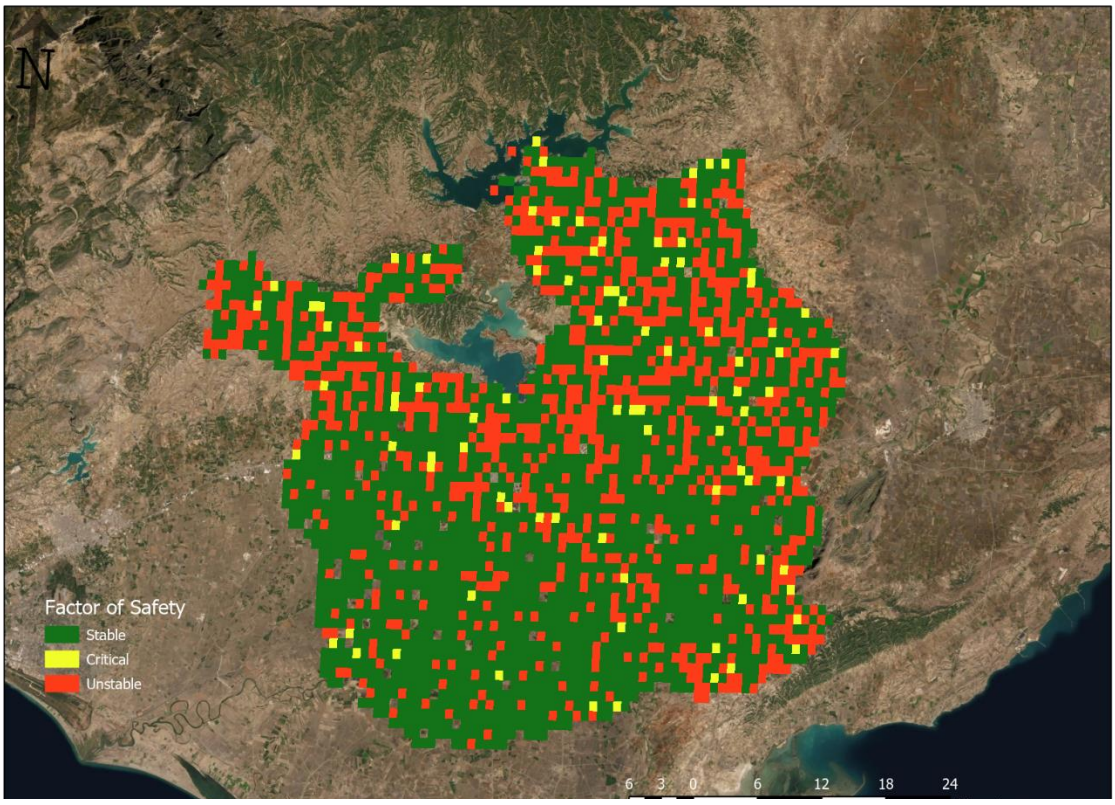

Figure 20. Landslide hazard map displayed in factor of safety per pixel.

The values of landslide are more evenly distributed over the area because of the presence of the water table in the equation. The water table is based on the flow accumulation tool in ArcGIS (figure 13), which accumulates flow as the accumulated weight of all cells flowing into each downslope cell in the output raster. This resulted in a raster map containing streams of high values in every depression in the digital elevation model (figure 21). In this map, a spectrum of values between zero (black in the map and dry) and one (white in the map and wet) are displayed for the entire study area. The combination of presence of water in valleys, where landslide hazard is lower than on slopes, the course data and the absence of any extremely sensitive regions, makes landslide hazard even more evenly distributed over the area.

Figure 19. Flow accumulation raster, showing all valleys in the DEM, distributing values of landslide hazard evenly over the area.

5.4 Risk

Risk is calculated by multiplying the mean damage ratio with the values of pixels. The mean damage ratio presents the percentage of the total value of a pixel that gets destroyed. Values of a pixel are determined by literature, housing prices and crop prices. These are displayed in figure 22.

The values are based on the land use patterns seen in figure 7. A significant gap can be noticed in the legend between the lightest green and yellow colors. The green colors represent agricultural and nature land use classes, valued between zero and 5000 euros per hectare. The yellow and red colors represent the urban areas, including infrastructure and industries. These are valued between one

million and four million euros per hectare. Even though the colors do not fully correspond, this map mimics the patterns of the land use map, since it is a direct descendant. The value map will influence the damage maps significantly in all three hazard types.

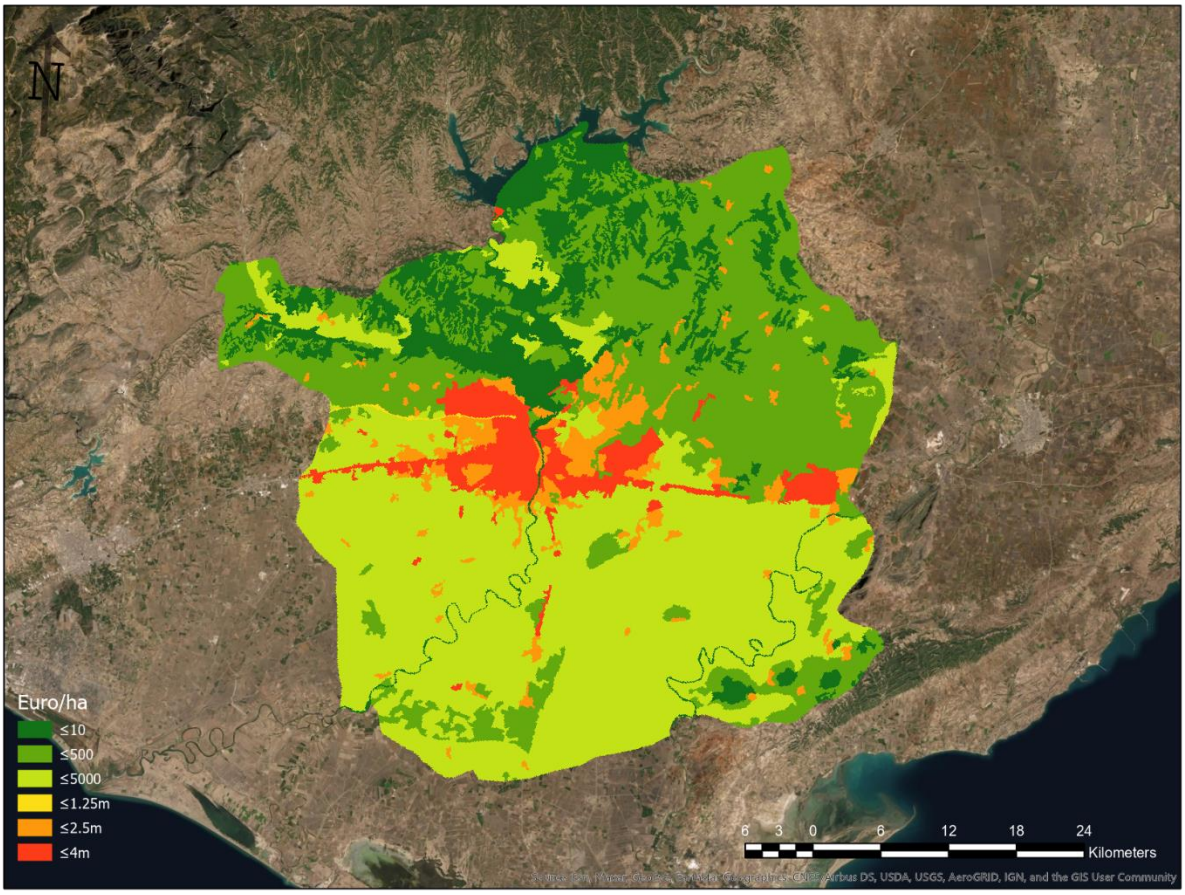

Figure 20. Monetary value per hectare of the study area in euros, based on literature, housing prices and crop prices.

5.4.1 Earthquake risk

The mean damage ratio of earthquakes is defined by equation 10. The input for this equation is in MMI format, which is not used in the earthquake hazard calculation (figure 17). To translate PGA into MMI, relation between the two is utilized (equation 11). Then, MDR is multiplied with the values in figure 20, which results in the map of figure 21.

A great similarity can be seen with figure 17. The damage values in the south of the city are higher due to their higher peak ground acceleration values (figure 17). The increasing PGA from north to south can also be noticed by the dark red spots south of the city of Adana, where villages with the same

values are located (figure 21). These villages have higher damage ratios because of their closeness to the shallow historical earthquakes and thus higher estimates of PGA values.

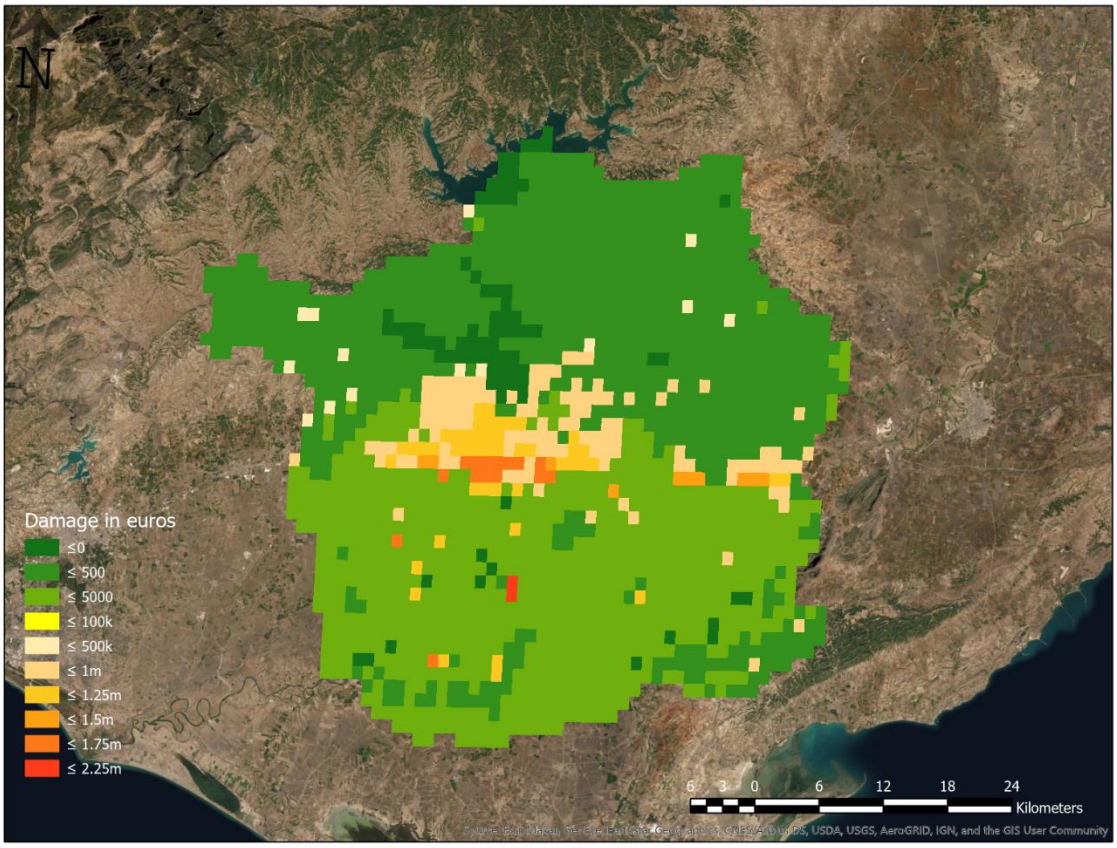

Figure 21. Earthquake risk map expressed in damages (euros) per hectare.

5.4.2 Flood risk

Flood hazard is based on the five parameters shown in table 3. The calculation shows great hazard in the city and surrounding villages, where the surfaced is paved. Also, the north seems to remain safe because of its steep slopes and high elevation (figure 22). To calculate the risk map, the value map in figure 20 needs to be multiplied with the mean damage ratio of floods in this area (equation 14).

The extent of paved surface is an extremely dominant factor in the calculation of flood risk since this increases both hazard and risk in itself. Hazard increases because of the very little infiltration paved surface offers. Risk increases because the value of paved surface is often higher than other land uses. A parallel can be drawn between the damage map of floods and the value of the pixels since a high value translates to high flood hazard. This is unique for floods. Earthquakes and landslides do not have such a relation between value of pixel and hazard of pixel. CN values of the land use classes influence flood hazard severely. As said, CN values are higher for pixels with a high percentage of paved surface. These are often urban areas, infrastructure related pixels or industrial areas. All three of these classes have high values compared to the other classes, which exist of pixels with agricultural purposes or wilderness.

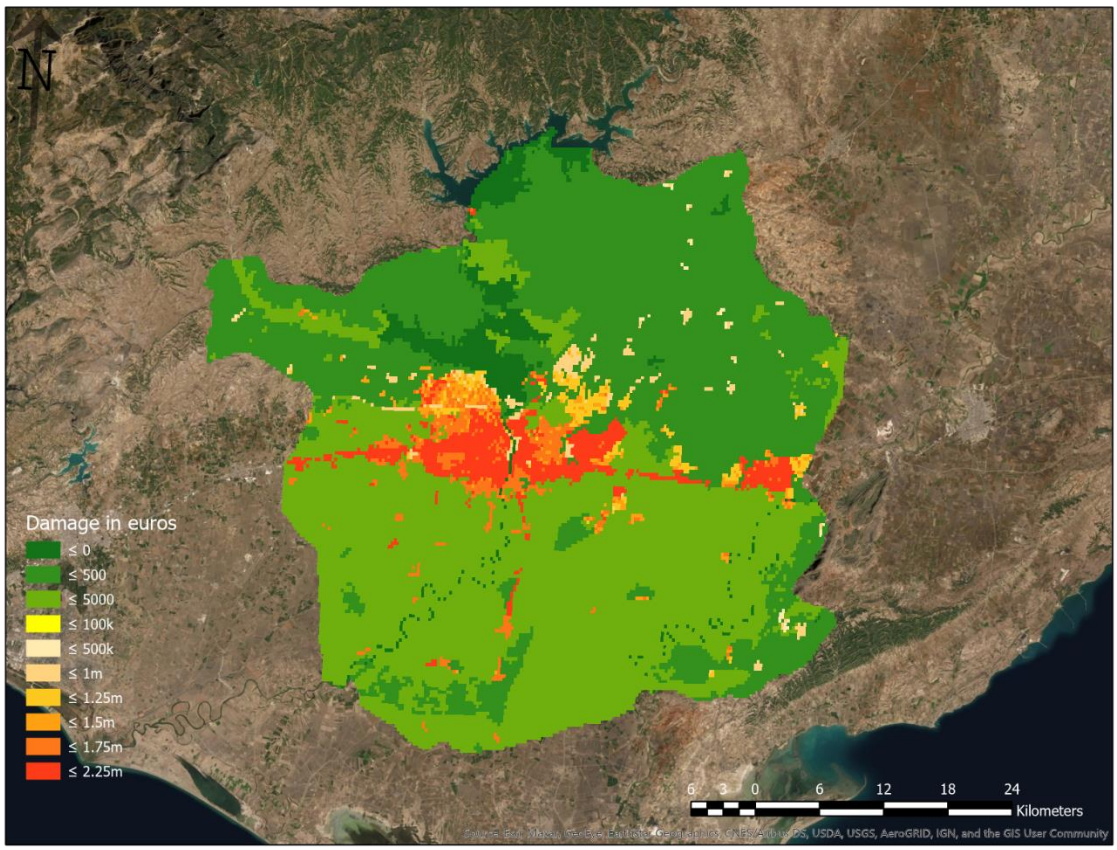

Figure 22. Flood damage in euros per hectare, based on flood hazard in figure 19 and the damage ratio of equation 14.

5.4.3. Landslide risk

Landslide risk is not as dependable on the value map as flood risk. Pixels with zero hazard do occur regularly on paved surface, resulting in a far more distributed map of risk. Landslide is always a far more local hazard than both flood and earthquakes. An event occurs can occur on a single pixel, while earthquakes and floods can extent their danger over hundreds of kilometers. This makes the patterns of landslide hazard and risk harder to explain. It is however interesting how the southern part of the area is almost risk free, while the city of Adana contains most unstable regions. Also, the Yakapınar village in the east has high potential damage due to the steep slopes.

The north, containing by far the most landslide hazard, is almost risk free. This is because of there are almost no objects at risk, since the steep slopes make it hard and, in some instances, impossible to build. While floods have a positive relation between hazard and risk, landslides seem to have a negative relation between the two (figure 23).

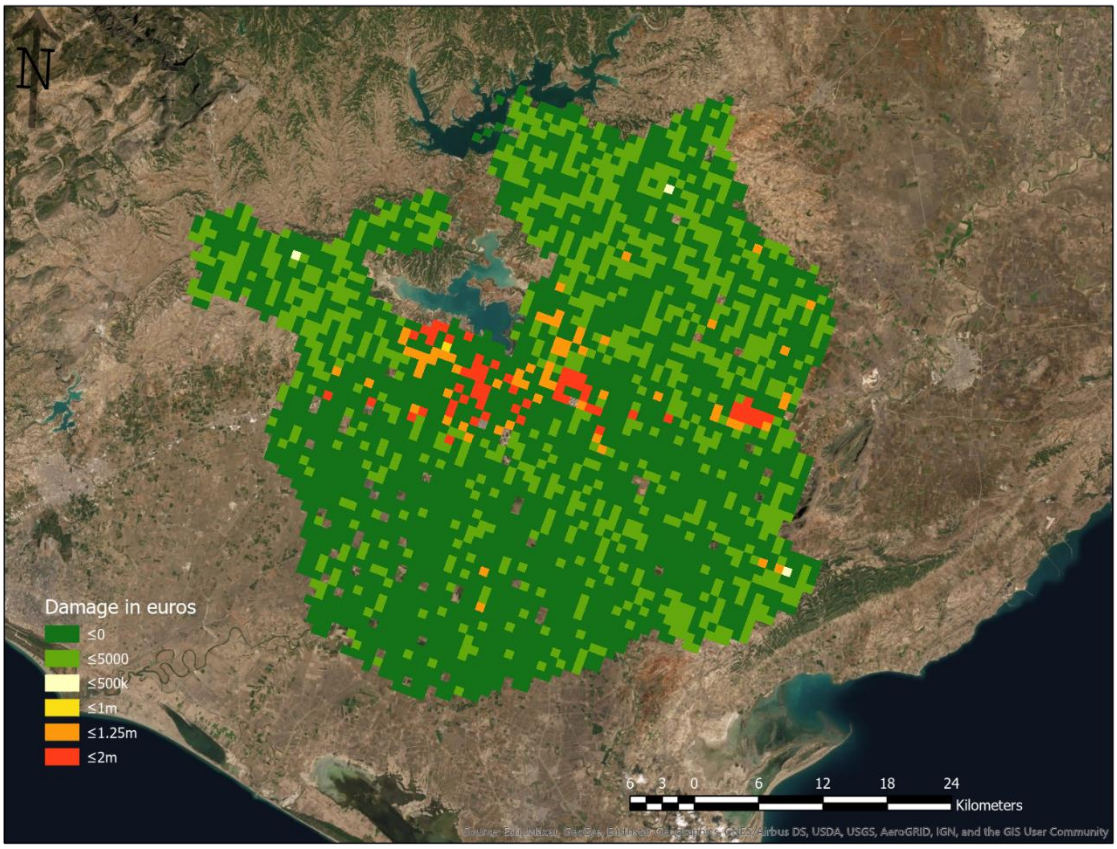

Figure 23. Landslide risk in the Adana area in euros per hectare.

6. Discussion

To easily compare and interpret the obtained results, the methodologies of each of the hazard and risk assessments are executed in a reasonably similar way. All final hazard maps can be interpreted as maps with high – and low hazard areas and since the risk calculation is done by multiplying the value per hectare and the level of hazard, a comparison in risk is possible as well.

6.1 Summary results

Earthquake hazard consists of two components. The first is calculating the recurrence interval and the second is calculating the spatial distribution of PGA values. The recognizable steep decline in recurrence interval is noticeable when increasing the magnitude. According to the graph, earthquakes with a magnitude larger than 6.0 are extremely rare in this area. The southern part of the study area is dominated by high PGA values, while a decrease in value occurs when going northwards. Increasing the magnitude fades the circular buffer zones with high PGA values in the south. The flood hazard map indicates that the steep and high north and south east contain little to no hazard, while the flat and fertile south contains most hazard. The same steep slopes, which were also noticeable in the flood hazard map, can be seen in the north and eastern part in the landslide hazard map, since these account for most of the unstable pixels. All risk maps have a very similar pattern based on the land use distribution of the study area. Differences between the hazards are the spatial distribution of high value pixels within urban environments and the fact that landslides are less dependent on land use distribution patterns.

6.2 Interpretation and implication

Concerning earthquake hazard, the southern part of the study area is dominated by high PGA values due to the softer soils and proximity to historic shallow earthquakes. Increasing the magnitude fades the circular buffer zones around these historic shallow earthquakes and creates a high to low pattern from south to north. A parallel can be drawn between the extend of the highest class of PGA values in T100 and the extend of vertisol soil in the area. PGA is based on the magnitudes obtained from the frequency-magnitude relation. The shape of the relation calculated in this research looks very similar to frequency-magnitude calculations based on earthquake inventory from other studies (Aki, 1987) (Cosentino, et al., 1977). It is however true that the shape of frequency-magnitude relations differs based on fault-type and earthquake depth (Pacheco, et al., 1992). Since earthquake depth is treated as an unknown factor in this study, only fault type is of importance when validating the relation. The Eastern Anatolian Fault is a transform fault zone where the Anatolian and Arabian plate slide against one another. The shape of the distribution of transform fault zones according to Pacheco, Scholz and Sykes is very similar to the frequency-magnitude relation generated in this research (Pacheco, et al.,

1992). The circular buffer zones around shallow historical earthquakes are a common sight in PGA estimation studies, since proximity to previous earthquakes play an important role in determining these peak ground acceleration values. An example is a study by Adnan & Harith, who estimated peak ground acceleration in Ranau, Malaysia by making use of an earthquake inventory. Different maps were created for different probabilities of exceedance, showing the same buffer zones around historical earthquakes and the same decrease in buffer patterns (Adnan & Harith, 2017) (figure 24).

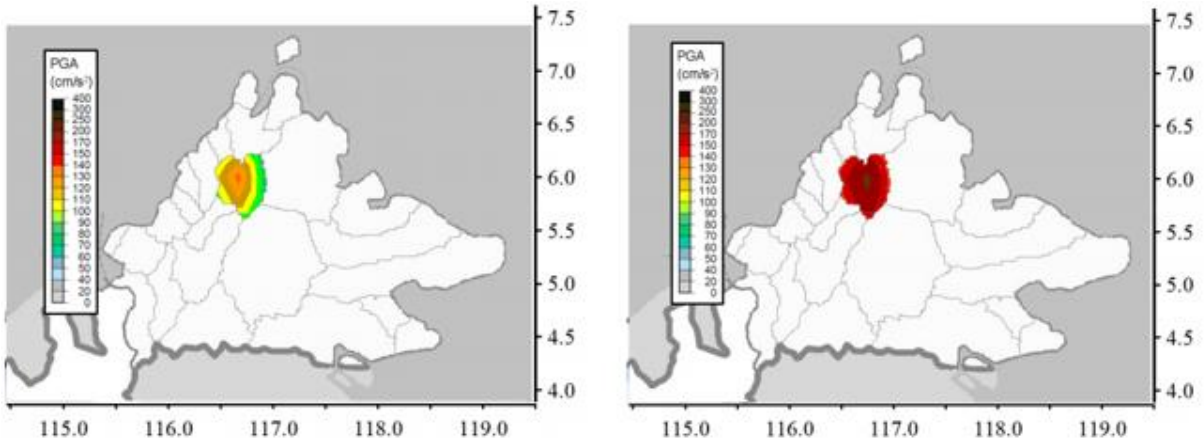

Figure 24. PGA hazard map calculated by Adnan & Harith for Ranau, Malaysia. On the left PGA is presented with a T of 475 and on the right PGA is presented with a T of 2475 (Adnan & Harith, 2017). The same buffer zones can be found around historical earthquakes as in this study, with the same decrease in buffer patterns.

Distribution of elevation in the study area dominates flow accumulation and slope patterns, and therefore accounts for a large part of the total flood hazard. The southern part of the study area is extremely flat, dominated by the thick vertisol soil profiles. The northern part, dominated by hard rock, has very steep slopes. Water therefore mainly flows southwards, accumulating on the vertisol plain. In the south east, a steep lone mountain range can be found resulting in the same process as in the north. Water flows from east to west accumulating in the vertisol plain. Based on this alone, the north is flood hazard free and the south would have trouble dealing with the accumulating water. These three variables account for seven out of the eleven weighting points of total flood hazard. The explaining factor is elevation. As said, the southern part of the area is prone to floods because of flow patterns determined by the digital elevation model. Besides the Curve Number method, DEMs are also often used to assess flood hazard. An obvious example is the study by Kourgialas and Karatzas, on which the flood assessment in this study is based on. The separate factors mentioned in figure 18 and the flood hazard map show similar results to their study, displaying the dominance of elevation (Kourgialas & Karatzas, 2011) (figure 25). Another explaining factor, of smaller significance, is the presence of impervious surface. It is hard for water to infiltrate the ground in areas with a high CN (Curve Number). The CN method is often used to study runoff and soil erosion and can also be used in flood hazard estimation (Chang, et al., 2009) (Jasrotia & Singh, 2006). When looking at the flood hazard map, areas

with high a high CN show increased flood hazard. CN explaining a significant part of flood hazard is a common phenomenon shown in multiple studies (Dawod, et al., 2011).

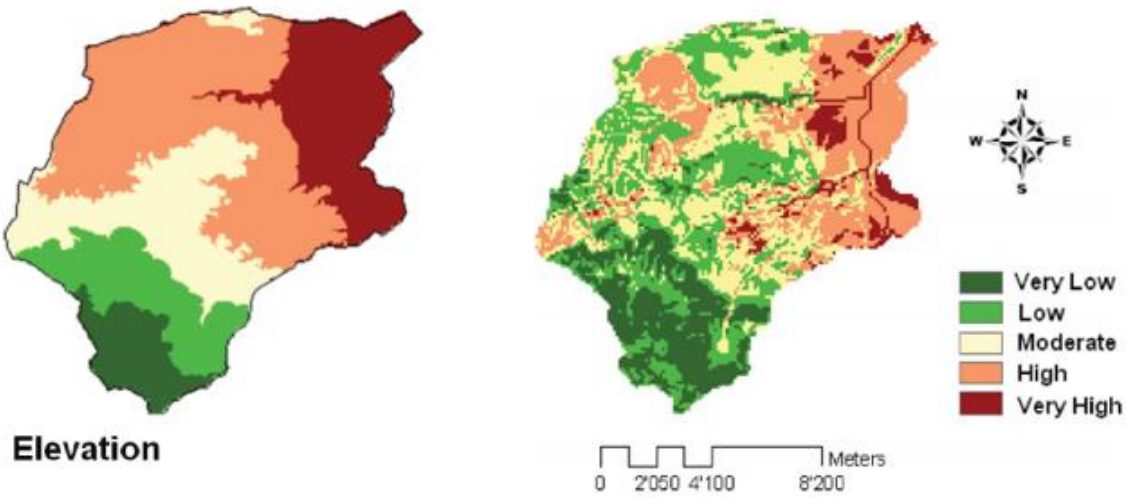

Figure 25. A comparison between elevation hazard vs total flood hazard in the study by Kourgialas and Karatzas (Kourgialas & Karatzas, 2011). Great similarity can be found between the two maps, similar to the results found in this study.

The steep slopes, which were also noticeable in the flood hazard map, can be seen in the north and eastern part, accounting for most of the unstable pixels in the landslide hazard map. The effective angle, cohesion and soil weight is highest for the vertisols in the south. This depolarizes the overall image, creating unstable slopes in the south as well. The values of landslide are even more evenly distributed over the area because of the presence of the water table in the equation. The water table is based on the flow accumulation tool in ArcGIS, which accumulates flow as the accumulated weight of all cells flowing into each downslope cell in the output raster. This resulted in a raster map containing streams of high values in every depression in the digital elevation model. Since most landslide estimations are based on landslide inventories, the results of landslide studies often have a higher resolution than the results of this study. Such a probabilistic approach, combined with the area's characteristics, also shows a more diverse map. Unstable slopes are clustered, while safe areas are also very recognizable. An example is a study by Mergili et al., where they evaluate the slope stability over a large number of slip surfaces based on landslide inventory. The same area characteristics are taken into account as in this study but including landslide inventory makes sure values are less evenly distributed and show more recognizable patterns (Mergili, et al., 2014). Another way to estimate landslide risk is by making use of a multi-criteria approach (MCA). This methodology was a more realistic alternative for this study, since it is especially useful for areas with limited data-availability. The difference between the approach used in this study and an MCA is the lack of assigned weights in this study. These weights are, in a way, implemented in the formula designed by Brunsden and Prior. This formula uses indicators as input, just as the MCA. Using an MCA for landslide assessment is

complicated since weights are very area specific. An example where the multi-criteria approach is used is in the 2008 paper by Abella, where a landslide risk assessment is conducted in Cuba. A very expert review of the area is needed before weights can be assigned. However, if this is reachable and data of indicators are reliant, extremely accurate results can be obtained (Abella, 2008).

Risk values are based on the land use patterns in the area. Even though the colors do not fully correspond, this map mimics the patterns of the land use map, since it is a direct descendant. The value map will influence the damage maps significantly in all three hazard types. It is relatively rare for risk assessments to make use of land cover as input for maximum potential damage value. For the three hazard types treated in this study, building inventories and population inventories are a more common source for risk estimations. In a study by Jena et al., earthquake risk is assessed for the Indonesian province of Aceh. In this research, a so-called network-analytic process model is constructed based on hazard probability and building inventory. This particular study is validated with an accuracy of 84 percent (Jena, et al., 2020). The availability of building inventories is important for accurately defining not only earthquake risk, but every type of risk.

For earthquakes, the damage values in the south of the city are higher due to their higher peak ground acceleration values. The increasing PGA from north to south can also be noticed by the dark red spots south of the city of Adana, where villages with the same values are located. These villages have higher damage ratios because of their closeness to the shallow historical earthquakes and thus higher estimates of PGA values. In the previously mentioned study by Jena et al., earthquake risk is calculated for a relatively densely populated area. Data is very accurate and in high resolution. In this thesis, the study area is relatively large. Data is scarce and there is a large spectrum with wilderness on one side and dense urban areas on the other side. Still, similarities between the results are noticeable. Patterns in land use, or building density, are visible in the final earthquake risk map. Bands of similar earthquake risk are however far more prominent in the study by Jena, since the previously mentioned spectrum of maximum potential damage values is smaller (Jena, et al., 2020) (figure 26).

For floods, the extent of paved surface is an extremely dominant factor in the calculation of flood risk since this increases both hazard and risk in itself. Hazard increases because of the very little infiltration paved surface offers. Risk increases because the value of paved surface is often higher than other land uses. This is unique for floods. Earthquakes and landslides do not have a positive relation between value of pixel and hazard of pixel. CN values of the land use classes influence flood hazard severely. Again, it is rare for studies to use land cover as input for maximum potential damage value. However,

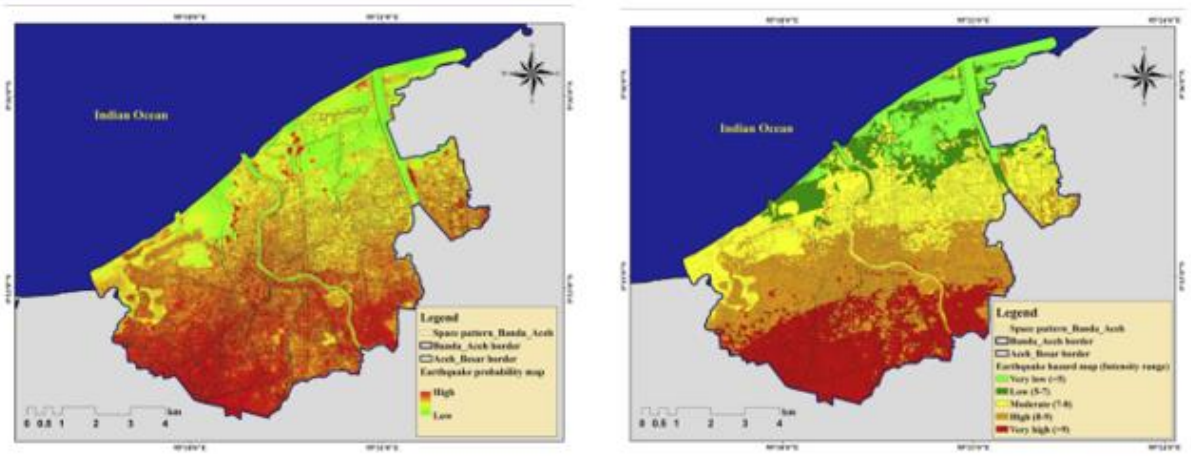

Figure 26. The small difference between earthquake hazard (left) and earthquake risk (right) when a small spectrum of value per pixel is being treated in a study (Jena, Pradhan, Beydoun, Sofyan, & Affan, 2020).

a study by Radwan, Alazba & Mossad did make use of land cover, in combination with population density and storm drainage data to estimate potential flood risk. A combination of flood hazard and vulnerability makes their flood risk map, showing a clear domination of vulnerability in this map (Radwan, et al., 2019). This domination of vulnerability is also visible in this study and can be declared to the positive relationship between vulnerability and hazard in floods (figure 27).

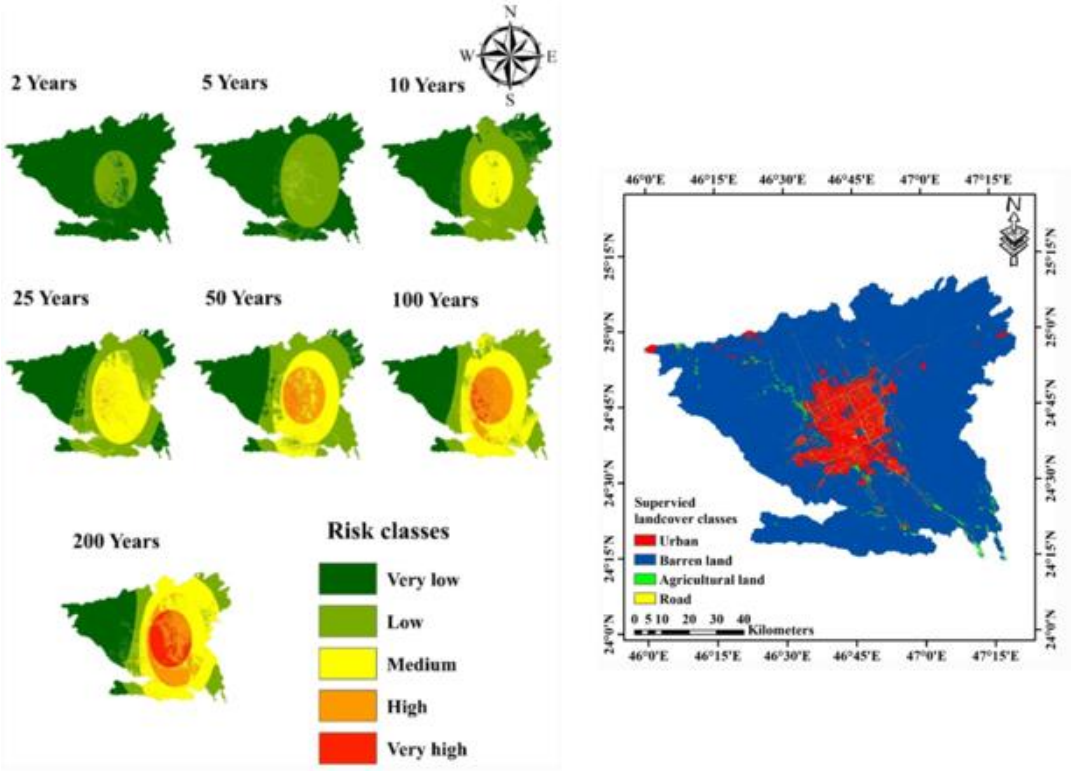

Figure 27. Risk is displayed on the left side, value of pixel is displayed on the right side (Radwan, Alazba, & Mossad, 2019). Similar to this study, the study by Radwan et al. shows the dominance of vulnerability in risk maps concerning flood hazard.

As noticed in the results chapter, landslide patterns are harder to explain compared to earthquakes and floods. Landslide risk is not as dependable on the value map as flood risk. Pixels with zero hazard do occur regularly on paved surface, resulting in a far more distributed map of risk. Landslides are always a far more local hazard than both flood and earthquakes. An event can occur on a single pixel, while earthquakes and floods can extent their danger over hundreds of kilometers. This makes the patterns of landslide hazard and landslide risk harder to explain. It is however interesting how the north, containing by far the most landslide hazard, is almost risk free. This is because of the lack of objects at risk, since the steep slopes make it hard and, in some instances, impossible to build. While floods have a positive relation between hazard and risk, landslides seem to have a negative relation between the two. Landslide risk assessments are often carried out on far more local scale than the scale used in this study. When using a smaller scale, individual buildings are identified and their characteristics are used for a vulnerability assessment, as is done in the study by Guillard-Gonçalves et al. (Guillard-Gonçalves, et al., 2016). A more similar approach to calculating risk compared to this research is conducted by Akgun, Kıncal & Pradhan. In this research, vulnerability is assessed by making use of landcover, assigning every pixel to either zero, no danger possible, or one, danger possible (Akgun, et al., 2011). This results in a risk map which is a one-on-one copy of the hazard map, limited to vulnerable areas. Since uniformness between hazard types is crucial for this study, an exception for landslides when it comes to vulnerability was not made, even when it might had been beneficial for portraying the results.

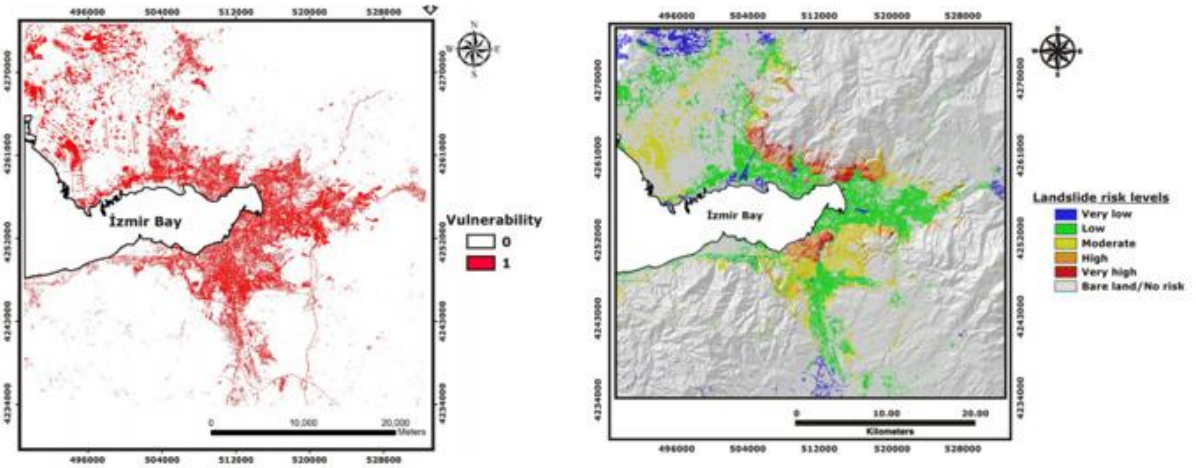

Figure 28. The risk map is a one on one copy of the hazard map, limited to vulnerable areas (Akgun, Kıncal, & Pradhan, 2011).

6.3 Limitations and recommendations

From the previous subchapter, a clear conclusion can be drawn. The methodology and data used for this research is excellent for assessing risk and a relatively large scale. Land use can be obtained globally on a relatively high resolution. Combining the calculated hazard with the widely available and very accessible land cover data is a great alternative for when the study area is large or when data is scarce. However, availability and accessibility have a negative relationship with accuracy, especially with landslide risk assessment. The studies mentioned in the previous subchapter which used building inventories show more accurate results on a higher resolution. Constructing such building inventories on such a large scale is hard but achievable. The easiest and least time-consuming way to do so it through remote sensing. Building characteristics can be obtained through aerial images, which can be used in earthquake, flood and landslide risk assessments. Many risk assessments are conducted making use of this methodology, but few use a multi-hazard approach or are executed on a large scale (Dong & Shan, 2013) (Thapa, et al., 2020) (Thennavan, et al., 2016). Using a multi-hazard approach on this scale will provide new insights in land use planning, hazard adaptation, hazard prevention and hazard mitigation.

7. Conclusion

This research is aimed to estimate earthquake, flood and landslide hazard and risk. This is done by calculating hazard separately for the three hazard types, with some hazards including feedbacks and interaction with other hazards. After these calculations, risk was estimated by applying hazard to a damage equation, resulting in three maps representing monetary values of loss.

The results for earthquake hazard show that the recognizable steep decline in recurrence interval is noticeable when increasing the magnitude. According to the frequency-magnitude relation, earthquakes with a magnitude larger than 6.0 are extremely rare in this area. The southern part of the study area is dominated by high PGA values, while a decrease in value occurs when going northwards. Increasing the magnitude fades the circular buffer zones with high PGA values in the south. The flood hazard map indicates that the steep and high north and south east contain little to no hazard, while the flat and fertile south contains most hazard. The same steep slopes, which were also noticeable in the flood hazard map, can be seen in the north and eastern part in the landslide hazard map, since these account for most of the unstable pixels. All risk maps have a very similar pattern based on the land use distribution of the study area. Differences between the hazards are the spatial distribution of high value pixels within urban environments and the fact that landslides are less dependent on land use distribution patterns.

The methodology and data used for this research is excellent for assessing risk and a relatively large scale. Land use can be obtained globally on a relatively high resolution. Combining the calculated hazard with the widely available and very accessible land cover data is a great alternative for when the study area is large or when data is scarce. However, availability and accessibility have a negative relationship with accuracy, especially with landslide risk assessment. The studies mentioned in the discussion which used building inventories show more accurate results on a higher resolution. Constructing such building inventories on such a large scale is hard but achievable. The easiest and least time-consuming way to do so it through remote sensing. Building characteristics can be obtained through aerial images, which can be used in earthquake, flood and landslide risk assessments. Many risk assessments are conducted making use of this methodology, but few use a multi-hazard approach or are executed on a large scale. Using a multi-hazard approach on this scale will provide new insights in land use planning, hazard adaptation, hazard prevention and hazard mitigation.

8. References

Abella, E. A. (2008). Multi-scale landslide risk assessment in Cuba. *Utrecht University*.

Adnan, A., & Harith, N. S. (2017). Estimation of peak ground acceleration of Ranau based on recent earthquake databases. *Malaysian Journal Geosciences*, 6-9.

Akgun, A., Kıncal, C., & Pradhan, B. (2011). Application of remote sensing data and GIS for landslide risk assessment as an environmental threat to Izmir city (west Turkey). *Environ Monit Assess*.

Aki, K. (1987). Magntiude-frequency relation for small earthquakes: A clue to the origin of f max of large earthquakes. *Journal of Geophysical Research*, 1349-1355.

Aktar, M., Ergin, M., Özalaybey, S., Tapirdamaz, C., Yörük, A., & Biçmen, F. (2000). A lower-crustal event in the northeastern Mediterranean: The 1998 Adana earthquake (Mw= 6.2) and its aftershocks. *Geophysical research letters*, 2361-2364.

Alcántara-Ayala, I. (2002). Geomorphology, natural hazards, vulnerability and prevention of natural disasters in developing countries. *Geomorphology*, 107-124.

Althuwaynee, O., & Pradhan, B. (2016). Semi-quantitative landslide risk assessment using GIS-based exposure analysis in Kuala Lumpur City. *Geomatics, Natural Hazards and Risk*, 706-732.

Ang, A. H.-S., & Tang, W. (1975). *Probability concepts in engineering planning and design.* John Wiley & Sons, Inc.

Askan, A., & Yucemen, M. (2010). Probabilistic methods for the estimation of potential seismic damage: Application to reinforced concrete buildings in Turkey. *Structural Safety*, 262-271.

ASTER. (2020, 11 1). Advanced Spaceborn Thermal Emission and Reflection Radiometer (ASTER).

Attorre, F., Alfo, M., De Sanctis, M., Francesconi, F., & Bruno, F. (2007). Comparison of interpolation methods for mapping climatic and bioclimatic variables at regional scale. *International Journal of Climatology*, 1825-1843.

Bauer, R. A., Kiefer, J., & Hester, N. (2001). Soil amplification maps for estimating earthquake ground motions in the Central US. *Engineering Geology*, 7-17.

Benito, G., Lang, M., Barriendos, M., Carmen Llasat, M., Francés, F., Ouarda, T., . . . Bobée, B. (2004). Use of systematic, palaeoflood and historical data for the improvement of flood risk estimation. Review of scientific methods. *Natural Hazards*, 623-643.

Boholm, Å. (2008). The public meeting as a theatre of dissent: risk and hazard in land use and environmental planning. *Journal of Risk Research*, 119-140.

Boore, D. (1987). The Prediction of Strong Ground Motion. *Strong Ground Motion Seismology*, 109-141.

Bostançı, B., Geymen, A., & Ilvan, A. (2017). GIS use in assessment of risky areas in natural disasters: The example of the Adana province. *UCTEA International Geographical Information Systems Congress 2017*, 15-18.

Brunsden, D., & Prior, D. (1984). *Slope instability.* Chichester: John Wiley.

Campbell, K. W. (1981). Near-source attenuation of peak horizontal acceleration. *Bulletin of the Seismological Society of America*, 2039-2070.

Cetin, M., Onoz, B., Aksoy, H., & Eris, E. (2018). Deriving accumulated precipitation deficits from drought severity-duration-frequency curves: A case study in Adana province, Turkey. *1st Internation Congress on Agricultural Structures and Irrigation, Proceedings and Abstracts Book, Antalya, Turkey*, 39-48.

Chang, H., Franczyk, J., & Kim, C. (2009). What is responsible for increasing flood risks? The case of Gangwon province, Korea. *Natural Hazards*, 339-354.

Chang, K., Chiang, S., & Hsu, M. (2007). Modeling typhoon-and earthquake- induced landslides in a mountainous watershed using logistic regression. *Geomorphology*, 335-437.

Cipollari, P., Schildgen, T. F., & Cosentino, D. (2013). Easternmost Mediterranean evidence of the Zanclean flooding event and subsequent surface uplift: Adana Basin, southern Turkey. *Geological Society*, 473-494.

Climate Data. (2020, September). *Adana*. Retrieved from climate-data: https://en.climate-data.org/asia/turkey/adana/adana-239/

Cosentino, P., Ficarra, V., & Luzio, D. (1977). Truncated exponential frequency-magnitude relationship in earthquake statistics. *Bulletin of the Seismological Society of America*, 1615-1623.

Crunch, C. (2008). Disaster data: A balanced perspective. *CRED*.

Cutter, S. L., & Finch, C. (2008). Temporal and spatial changes in social vulnerablity to natural hazards. *Proceedings of the National Academy of Sciences*, 2301-2306.

Dai, F., Lee, C., & Ngai, Y. (2002). Landslide risk assessment and management: an overview. *Engineering Geology*, 65-87.

Dawod, G. M., Mirza, M. N., & Al-Ghamdi, K. A. (2011). GIS-based spatial mapping of flash flood hazard in Makkah City, Saudi Arabia. *Journal of Geographic Information System*, 225-231.

de Vugt, L. C. (2018). Mapping and modelling of landslide and flood hazards on St. Eustatius with openLISEM. *Master thesis*.

Delmonaco, G., Leoni, G., Margottini, C., Puglisi, C., & Spizzichino, D. (2003). Large scale debris-flow hazard assessment: a geotechnical approach and GIS modelling. . *Natural Hazards and Earth System Science*, 443-455.

Demirören News Agency. (2019, December 25). *Flash floods paralyze Turkey's southern province Adana.* Retrieved from hurriyetdailynews.com: https://www.hurriyetdailynews.com/flash-floods-paralyze-turkeys-southern-province-of-adana-150264

Dokka, R. (2006). Modern-day tectonic subsidence in coastal Louisiana. *Geology*, 281-284.

Dong, L., & Shan, J. (2013). A comprehensive review of earthquake-induced building damage detection with remote sensing techniques. *ISPRS Journal of Photogrammetry and Remote Sensing*, 85-99.

Douglas, J. (2007). Physical vulnerability modelling in natural hazard risk assessment. *Natural Hazards and Earth System Sciences*, 283-288.

Elliott, J. (2020). Earth observation for the assessment of earthquake hazard, risk and disaster management. *Surveys in geophysics*, 1323-1354.

Encyclopaedia Brittanica. (2016, November 2016). *Luvisol*. Retrieved from Brittanica.com: https://www.britannica.com/science/Luvisol

ESRI. (2020, 1 19). *How flow accumulation works*. Retrieved from pro.arcgis.com: https://pro.arcgis.com/en/pro-app/latest/tool-reference/spatial-analyst/how-flow-accumulation-works.htm

Fan, X., Scaringi, G., Korup, O., West, A., van Westen, C., & Tanyas, H. (2019). Earthquake-induced chains of geolocig hazards: Patterns, mechanisms and impacts. *Reviews of Geophysics*, 57.

Finlay, P., & Fell, R. (1997). Landslides: Risk perception and acceptance. *Canadian Geotechnical Journal*, 169-188.

Fuchs, S., & Thaler, T. (2018). *Vulnerability and resilience to natural hazards.* Cambridge University Press.

Fuchs, S., Heiss, K., & Hübl, J. (2007). Towards an empirical vulnerability function for use in debris flow risk assessment. *Nat. Hazards. Earth. Syst. Sci.*, 495-506.

Fukushima, Y., & Tanaka, T. (1990). A new attenuation relation of peak horizontal acceleration of strong earthquake in Japan. *Bull. Seism. Soc. Am.* , 757-783.

Ghasemi, P., Khalili-Damghani, K., Hafezalkotob, A., & Raissi, S. (2020). Stochastic optimization model for distribution and evacuation planning (a case study of Tehran earthquake). *Socio-Economic Planning Sciences*.

Gill, J., & Malamud, B. (2014). Reviewing and visualizing the interactions of natural hazards. *Rev. Geophys.*, 680-722.

Global Facility for Disaster Reduction and Recovery. (2016). *The making of a riskier future: How our decisions are shaping future disaster risk.* GFDRR.

Gorum, T., Fan, X., van Westen, C., Huang, R., Xu, Q., Tang, C., & Wang, G. (2011). Distribution pattern of earthquake induced landslides triggered by the 12 May 2008 Wenchuan earthquake. *Geomorphology*, 152-167.

Guillard-Gonçalves, C., Zêzere, J. L., Pereira, S., & Garcia, R. A. (2016). Assessment of physical vulnerability of buildings and analysis of landslide risk at the municipal scale: application to the Loures municipality, Portugal. *Natural Hazards & Earth System Sciences*.

Gunturi, S. (1993). *Building-specific earthquake damage estimation.* Stanford University.

Gutenberg, B., & Richter, C. (1944). Frequency of earthquakes in California. *Bull. Seismol. Soc. Am.* , 185-188.

Harp, E., & Jibson, R. W. (1996). Landslides triggered by the 1994 Northridge, California, earthquake. *Bulletin of the seismological society of America*, 319-332.

Hashemi, M., & Alesheikh, A. A. (2011). A GIS-based earthquake damage assessment and settlement methodology. *Soil Dynamics and Earthquake Engineering*, 1607-1617.

Havskov, J., & Ottemöller, L. (2010). *Routine data processing in earthquake seismology.* Springer Netherlands.

Hong, Y., Adler, R. F., Negri, A., & Huffman, G. J. (2007). Flood and landslide applications of near real-time satellite rainfall products. *Natural Hazards*, 285-294.

Huizinga, J., de Moel, H., & Szewczyk, W. (2017). Global flood depth-damage functions: Methodology and the database with guidelines. *Joint research centre (Seville site)*.

Hürriyet. (2019, December 25). Flash floods paralyze Turkey's southern province of Adana. *Hürriyet*.

Inbar, M. (2020). Effects of a high magnitude flood in a Mediterranean climate: A case study in the Jordan River basin. *Catastrophic Flooding: Binghamton Geomorphology Symposium 18*.

IPCC. (2012). *Managing the risks of extreme events and disasters to advance climate change adoption.* New York: CAMBRIDGE UNIVERSITY PRESS.

Irwansyah, E., Winarko, E., Rasjid, Z. E., & Bekti, R. (2013). Earthquake hazard zonation using peak ground acceleration (PGA) approach. *Journal of Physics: Conference Series*.

ISRIC. (2020, 11 10). *soilgrids*. Retrieved from soilgrids.org: https://soilgrids.org/

Jasrotia, A., & Singh, R. (2006). Modeling runoff and soil erosion in a catchment area, using the GIS, in the Himalayan region, India. *Environmental Geology*, 29-37.

Jena, R., Pradhan, B., Beydoun, G., Sofyan, H., & Affan, M. (2020). Integrated model for earthquake risk assessment using neural network and analytic hierarchy process: Aceh province, Indonesia. *Geoscience Frontiers*, 613-634.

Kalyoncuoglu, U. Y. (2007). Evaluation of seismicity and seismic hazard parameters in Turkey and surrounding area using a new approach to the Gutenberg-Richter relation. *J Seismol*, 131-148.

Kappes, M. S., Keiler, M., von Elverfeldt, K., & Glade, T. (2012). Challenges of analyzing multi-hazard risk: a review. *Natural Hazards*, 1925-1958.

Kappes, M., Gruber, K., Frigerio, S., Bell, R., Keiler, M., & Glade, T. (2012). The MultiRISK platform: The technical concept and application of a regional-scale multihazard exposure analysis tool. *Geomorphology*, 139-155.

Keller, E. A., & DeVecchio, D. E. (2015). *Natural Hazards.* New York: Routledge.

Kirchsteiger, C. (1999). On the use of probabilistic and deterministic methods in risk analysis. *Journal of Loss Prevention in the Process Industries*, 399-419.

Kourgialas, N. N., & Karatzas, G. (2011). Flood management and a GIS modelling method to assess flood-hazard areas—a case study. *Hydrological Sciences Journal*, 212-225.

Kuru, T., & Ulusay, R. (2004). 1998 Adana-Ceyhan (Turkey) earthquake and a preliminary microzonation Based on liquefaction potential for Ceyhan Town. *Natural Hazards*, 59-88.

Leventeli, Y. (2016). Sarisih landslide in Trans-European motorway (Pozanti, Adana, Turkey). *International Multidisciplinary Scientific GeoConference: SGEM*, 253-260.

Linkimer, L. (2008). Relationship between peak ground acceleration and Modified Mercali Intensity in Costa Rica. *Revista Geológica de América Central*, 81-94.

McBean, G. (2004). Climate change and extreme weather: A basis for action. *Natural Hazards*, 177-190.

Mergili, M., Marchesini, I., Rossi, M., Guzzetti, F., & Fellin, W. (2014). Spatially distributed three-dimensional slope stability modelling in a raster GIS. *Geomorphology*, 178-195.

Meroni, F., Squarcina, T., Pessina, V., Locati, M., Modica, M., & Zoboli, R. (2017). A damage scenario for the 2012 Northern Italy Earthquakes and estimation of the economic losses to residential buildings. *International Journal of Disaster Risk Science*, 326-341.

Miyakoshi, J., Hayashi, Y., Tamura, K., & Fukuwa, N. (1997). Damage ratio functions of buildings using damage data of the 1995 Hyogo-Ken Nanbu earthquake. *7th International Conference on Structural Safety and Reliability (ICOSSAR '97)*, 349-354.

Morgan, R. (2005). *Soil erosion and conservation.* Oxford: Blackwell Publishing Ltd.

Munich Re. (2019, September 23). *Extreme storms, wildfires and droughts cause heavy nat cat losses in 2018*. Retrieved from munichre.com: https://www.munichre.com/en/media-relations/publications/press-releases/2019/2019-01-08-press-release/index.html

Murphy, J., & O'Brien, L. (1977). The correlation of peak ground acceleration amplitude with seismic intensity and other physical parameters. *Bull. Seismol. Soc. Amer.*, 877-915.

NASA . (2020, 11 01). Depth of soil, Earthdata.

Nishenko, S. P. (1985). Seismic potential for large and great interplate earthquakes along the Chilean and southern Peruvian margins of South America: a quantitative reappraisal. *Journal of Geophysical Research: Solid Earth*, 3589-3615.

Numbeo. (2020, 12 4). *Property prices in Adana, Turkey.* Retrieved from numbeo.com: https://www.numbeo.com/property-investment/in/Adana

Oberndofer, S., Sander, P., & Fuchs, S. (2020). Multi-hazard risk assessment for roads: Probabilistic versus deterministic approaches. *Natural Hazards and Earth System Sciences*, 2020-2066.

O'Brien, K., & Leichenko, R. (2003). Winners and losers in the context of climate change. *Annals of the American Association of Geographers*, 89-103.

Pacheco, J., Scholz, C., & Sykes, L. (1992). Changes in frequency-size relationship from small to large earthquakes. *Nature*, 71-73.

Papathoma-Köhle, M., Zischg, A., Fuchs, S., Glade, T., & Keiler, M. (2015). Loss estimation for landslides in mountain areas- An integrated toolbox for vulnerability assessment and damage documentation. *Environmental Modelling & Software*, 156-169.

Pardeshi, S. D., Autade, S. E., & Pardeshi, S. S. (2013). Landslide hazard assessment: recent trends and techniques. *SpringerPlus*, 523.

Pearce, A. J., & O'Loughlin, C. L. (1985). Landsliding during a M 7.7 earthquake: influence of geology and topography. *Geology*, 855-858.

Pellicani, R., van Westen, C., & Spilotro, G. (2014). Assessing landslide exposure in areas with limited landslide information. *Landslides*, 463-480.

Pfister, L., Kwadijk, J., Musy, A., Bronstert, A., & Hoffmann, L. (2004). Climate change, land use change and runoff prediction in the Rhine-Meuse basin. *River Research and Applications*, 229-241.

Polemio, M., & Petrucci, O. (2000). Rainfall as a landslide triggering factor an overview of recent international research. *Landslides in research, theory and practice*.

Radeff, G., Schildgen, T. F., Cosentino, D., Strecker, M. R., Cipollari, P., Darbaş, G., & Gürbüz, K. (2017). Sedimentary evidence for late Messinian uplift of the SE margin of the Central Anatolian Plateau: Adana Basin, southern Turkey. *Basin Research*, 488-514.

Radwan, F., Alazba, A. A., & Mossad, A. (2019). Flood risk assessment and mapping using AHP in arid and semiarid regions. *Acta Geophysica*, 215-229.

Ram, T. D., & Guoxin, W. (2013). Probabilistic seismic hazard analysis in Nepal. *Earthquake engineering and engineering vibration*, 577-586.

Richter, C., & Gutenberg, B. (1942). Earthquake magnitude, intensity, energy, and acceleration. *Bull. Seismol. Soc. Amer.*, 163-191.

Ritchie, H., & Roser, m. (2019, November). *Natural Disasters*. Retrieved from Our World in Data: https://ourworldindata.org/natural-disasters

Romali, N. (2019). Flood damage function model for residential area in Kuantan: A preliminary study. *International journal of integrated engineering*.

Schenk, V., Schenková, Z., Kottnauer, P., Guterch, B., & Labák, P. (2000). Earthquake hazard for the Czech Republic, Poland and Slovakia. *Natural Hazards*.

Schwarz, M., Preti, F., Giadrossich, F., Lehmann, P., & Or, D. (2010). Quantifying the role of vegetation in slope stability: A case study in Tuscany (Italy). *Ecological Engineering*, 285-291.

Seçkin, N., & Topçu, E. (2016). Adana ve çevre illerde gözlenen yıllık maksimum yağışların bölgesel frekans analizi. *Journal of the Faculty of Engineering and Architecture of Gazi University*, 1049-1062.

Seed, H., & Idriss, I. (1969). Influence of soil conditions on ground motions during earthquakes. *Journal of the Soil Mechanics and Foundations Division*, 99-137.

Semblat, J., Kham, A., Parara, E., Bard, P., Pitilakis, K., Makra, K., & Raptakis, D. (2005). Seismic wave amplification: Basin geometry vs soil layering. *Soil dynamics and earthquake engineering*, 529-538.

Shaban, A., Khawlie, M., & Bou Kheir, R. A. (2001). Assessment of road instability along a typical mountainous road using GIS and aerial photos, Lebanon–eastern Mediterranean. *Bull. Engng. Environ.*, 93-101.

Sidle, R., & Swanston, D. (1982). Analysis of a small debris slide in coastal Alaska. *Can Geotech J*, 167-174.

Sivrikaya, O., Yalcin, M. G., & Kilic, A. M. (2008). The 2001 Adana landslide and its destructive effects, Turkey. *Environmental Geology*, 1489-1500.

Smith, K., & Ward, R. (1998). *Floods: physical processes and human impacts.* Jon Wiley and Sons Ltd.

Smith, R. (1986). Comparing traditional methods for selecting class Intervals on choropleth maps. *The Profess. Geogr.*, 62-67.

Spence, W. (1977). Measuring the size of an earthquake. *Earthquake Information Bulletin*, 21-23.

Swiss Standard. (n.d.). *SN 670 010b, Characteristic coefficients of soils.* Association of Swiss Road and Traffic Engineers.

Tanoğlu. (1943). *Türkiye'de Büyük Su İşlerinin.* Istanbul.

Tate, E., & Cutter, S. L. (2010). Ingegrated multihazard mapping. *Environment and Planning B: Planning and Design*, 646-663.

Terlien, M. (1998). The determination of statistical and deterministic hydrological landslide-triggering thresholds. *Environmental geology*, 124-130.

Terzi, S., Torresan, S., Schneiderbauer, S., Critto, A., Zebisch, M., & Marcomini, A. (2019). Multi-risk assessment in mountain regions: a review of modelling approaches for climate change adaption. *J. Environ. Manag.*, 759-771.

Thapa, S., Shrestha, A., Lamichhane, S., Adhikari, R., & Gautam, D. (2020). Thapa, S., Shrestha, A., Lamichhane, S., Adhikari, R., & Gautam, D. (2020). Catchment-scale flood hazard mapping and flood vulnerability analysis of residential buildings: The case of Khando River in eastern Nepal. *Journal of Hydrology: Regional Studies*.

The Courier-Mail. (1947, November 11). 200 DIE IN FLOODS. *The Courier-Mail*, p. 1.

Thennavan, E., Ganapathy, G. P., Sekaran, S. C., & Rajawat, A. S. (2016). Thennavan, E., Ganapathy, G. P., Sekaran, S. C., & Rajawat, A. S. (2016). Use of GIS in assessing building vulnerability for landslide hazard in The Nilgiris, Western Ghats, India. *Natural Hazards*, 1031-1050.

Totschnig, R., Sedlacek, W., & Fuchs, S. (2011). A quantitative vulnerability function for fluvial sediment transport. *Nat. Hazards*, 681-703.

Tozoglu, A. E. (2020). A chapter in the modernization of Turkey: damming the rivers, claiming the natural landscape, and building of the Seyhan Dam in Cicilia. *Turkish Studies*.

Trifunac, M., & Brady, A. (1975). On the correlation of seismic intensity scale with the peaks of recorded strong ground motion. *Bull. Seismol. Soc. Amer.*, 139-162.

Turcotte, D., Malamud, B., Guzzetti, F., & Reichenbach, P. (2006). A general landslide distribution applied to a small inventory in Todi, Italy. *Geological Society, London*, 105-111.

Ulusay, R., Tuncay, E., Sonmez, H., & Gokceoglu, C. (2004). An attenuation relationship based on Turkish strong motion data and iso-acceleration map of Turkey. *Engineering Geology*, 265-291.

USGS. (2020, 11 10). *USGS Earthquake Catalog*. Retrieved from earthquake.usgs.gov: https://earthquake.usgs.gov/earthquakes/search/

van Westen, C., van Asch, T., & Soeters, R. (2006). Landslide hazard and risk zonation - why is it still so difficult? *Bull Eng Geol Environ*, 167-184.

Varnes, D. J. (1984). *Landslide Hazard zonation: a review of principles and practice.*

Wahlström, R., Tyagunov, S., Grünthal, G., Stempniewski, L., Zschau, J., & Müller, M. (2004). Seismic risk analysis for Germany: methodology and preliminary results. *Disasters and society from hazard risk assessment to risk reduction: proceedings of the international conference*, 83-90.

Wenk, T., Lacave, C., & Peter, K. (1998). The Adana-Ceyhan earthquake of June 27, 1998. *Swiss society for earthquake engineering and structural dynamics*.

Wheater, H., Chandler, R., Onof, C., Isham, V., Bellone, E., Yang, C. L., . . . Segond, M.-L. (2005). Spatial-temporal rainfall modelling for flood risk estimation. *Stochastic environmental research and risk assessment*, 403-416.

Winter, B., Schneeberger, K., Huttenlau, M., & Stötter, J. (2018). Sources of uncertainty in a probabilistic flood risk model. *Natural Hazards*, 431-446.

Youssef, A., Pradhan, B., & Hassan, A. (2011). Flash flood risk estimation along the St. Katherine road, southern Sinai, Egypt using GIS based morphometry and satellite imagery. *Environmental earth sciences*, 611-623.

9. Annex

I. Earthquake hazard GIS flowchart

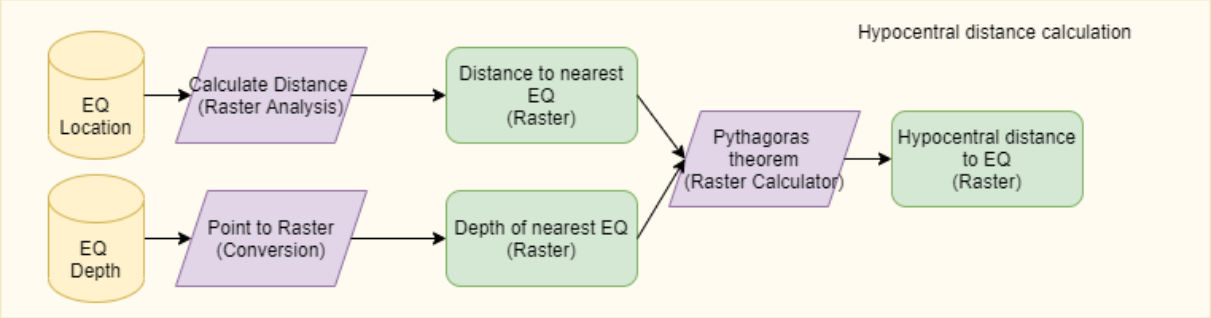

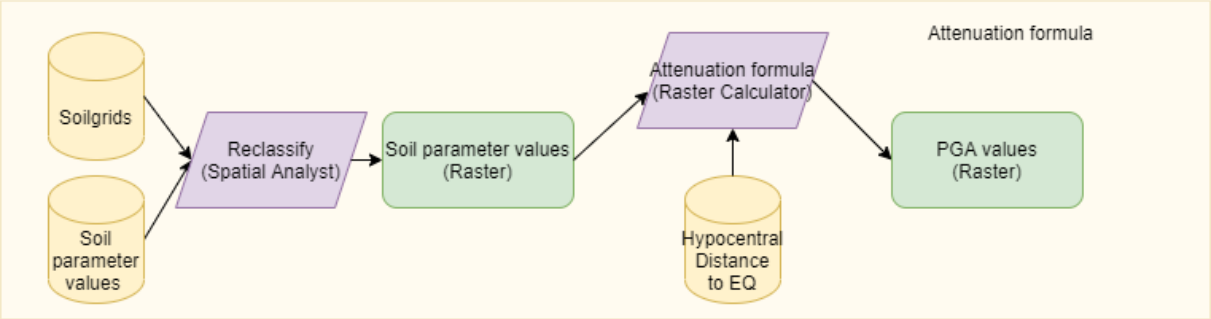

II. Flood hazard GIS flowchart

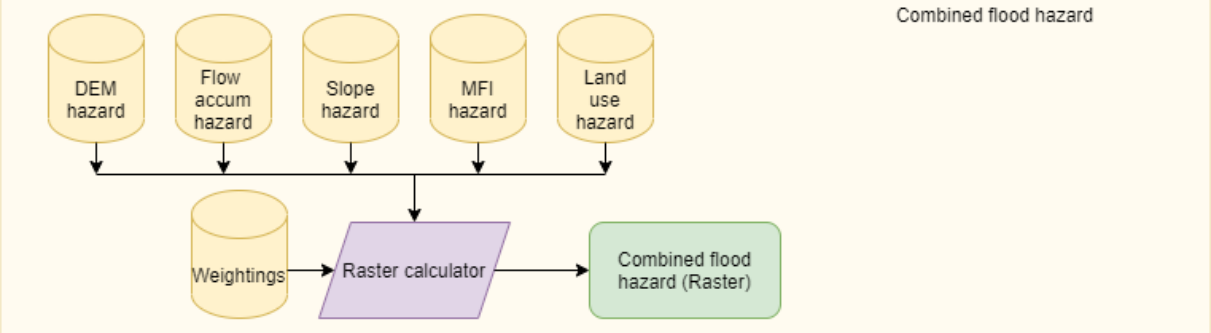

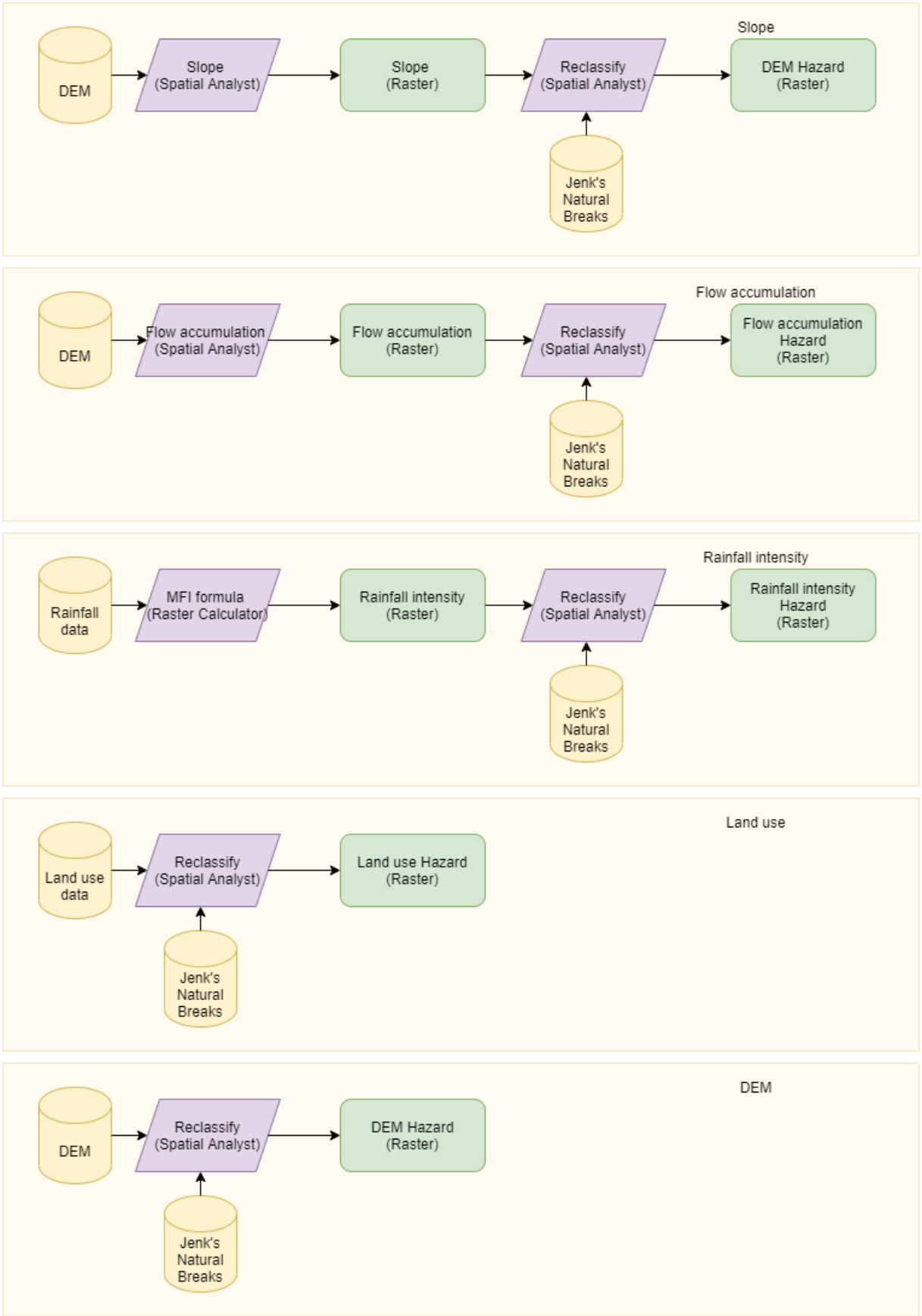
Slope
DEM
Slope (Spatial Analyst)
Slope (Raster)
Reclassify (Spatial Analyst)
DEM Hazard (Raster)
Jenk's Natural Breaks
Flow accumulation
DEM
Flow accumulation (Spatial Analyst)
Flow accumulation (Raster)
Reclassify (Spatial Analyst)
Flow accumulation Hazard (Raster)
Jenk's Natural Breaks
Rainfall intensity
Rainfall data
MFI formula (Raster Calculator)
Rainfall intensity (Raster)
Reclassify (Spatial Analyst)
Rainfall intensity Hazard (Raster)
Jenk's Natural Breaks
Land use
Land use data
Reclassify (Spatial Analyst)
Land use Hazard (Raster)
Jenk's Natural Breaks
DEM
DEM
Reclassify (Spatial Analyst)
DEM Hazard (Raster)
Jenk's Natural Breaks

III. Landslide hazard GIS flowchart

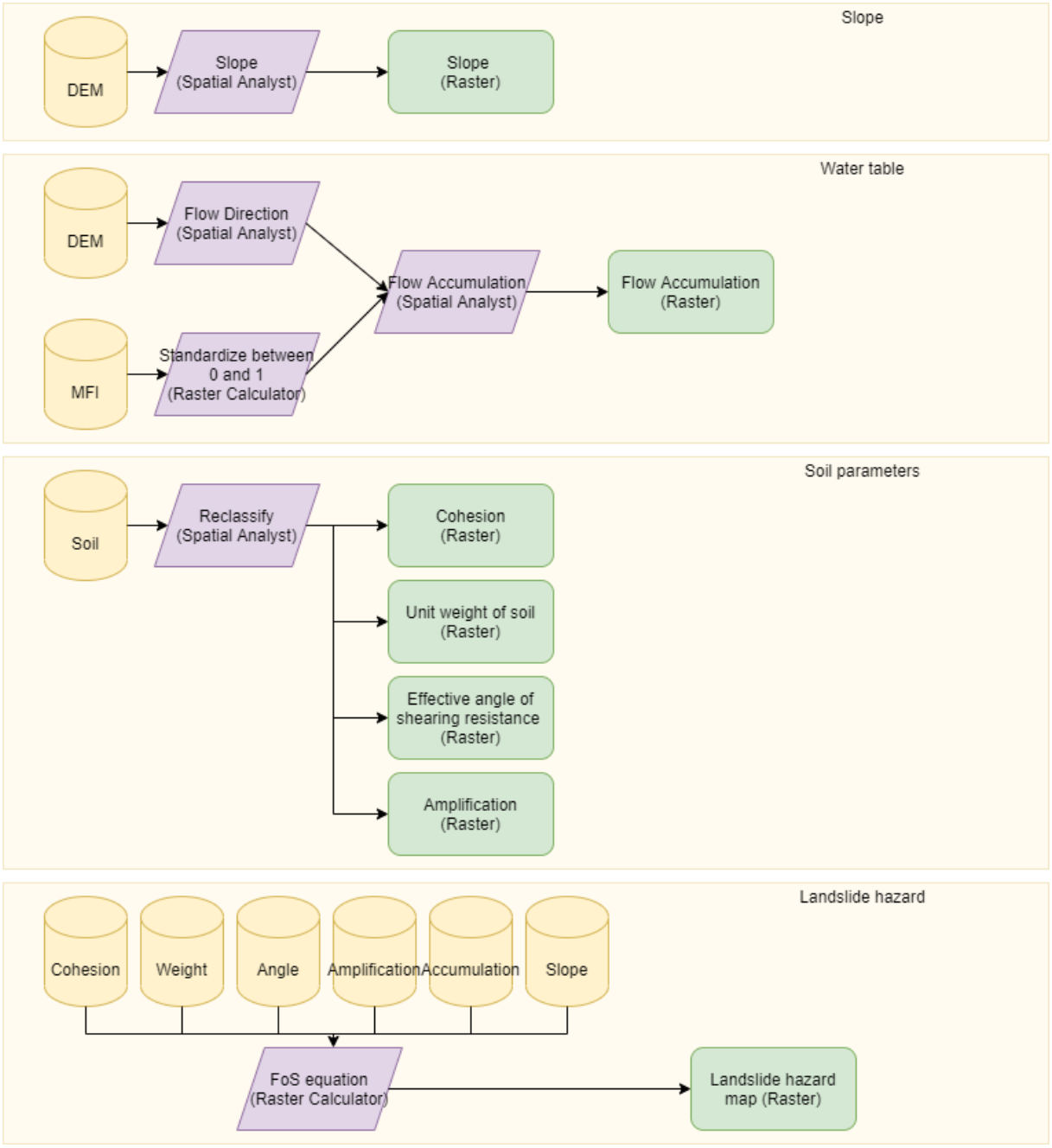

IV. Risk GIS flowchart

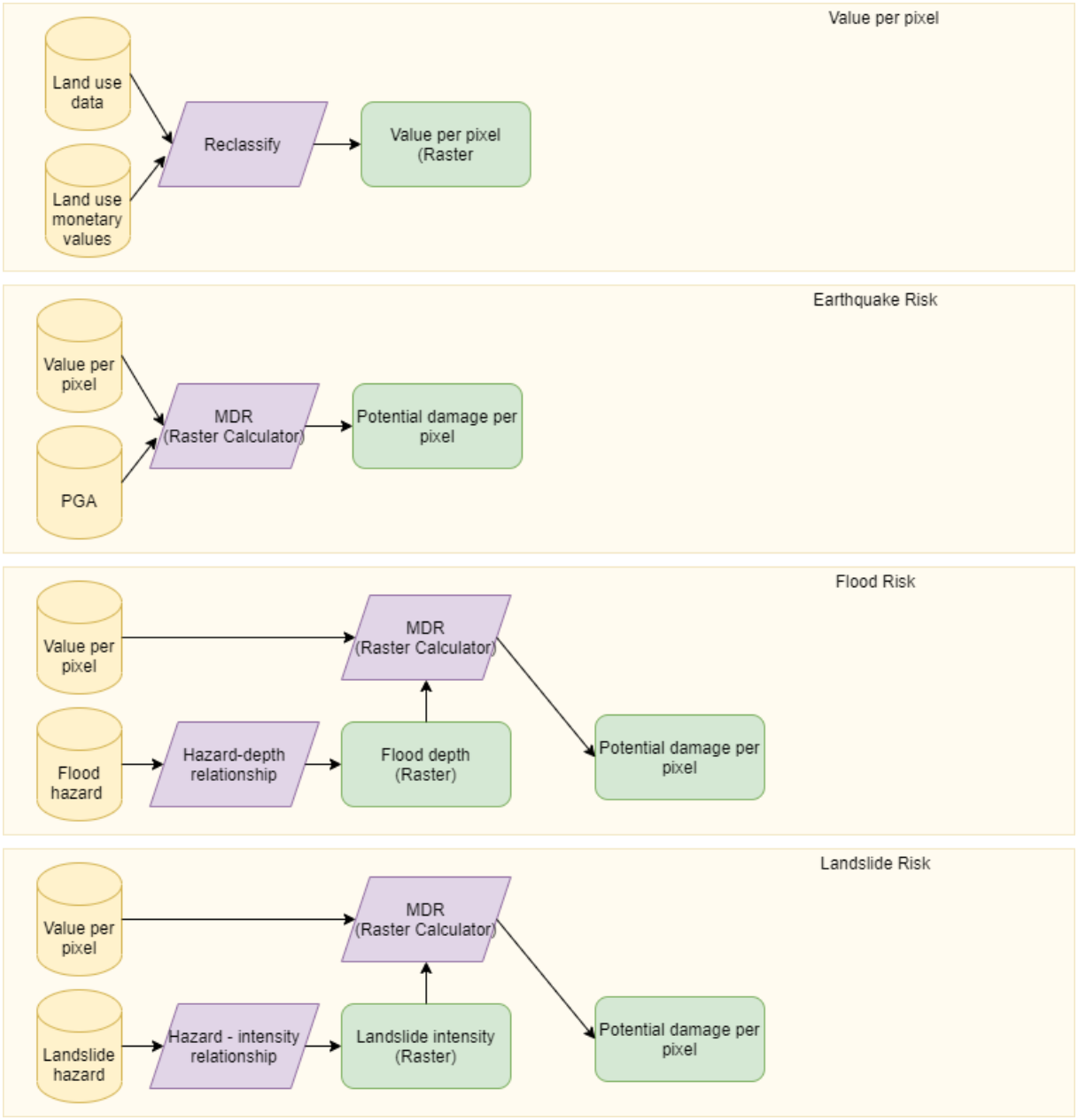

V. List of figures

VI. List of tables

VII. List of equations